

**POLITECNICO DI TORINO**

**Master's Degree in Aerospace Engineering**



**Master's Degree Thesis**

**Numerical analysis of a water  
Loss-Of-Coolant-Accident inside  
the EU DEMO Vacuum Vessel**

**Supervisors**

**Dr. ANTONIO FROIO**

**Dr. ANDREA ZAPPATORE**

**Candidate**

**LEONARDO RUIU**

**DECEMBER 2021**



# Abstract

Nuclear fusion is one of the few technologies with the potential to answer the global need for a reliable, sustainable, carbon-free, electricity source. Europe efforts to advance nuclear fusion research are coordinated by the EUROfusion Consortium, that with the "European Research Roadmap to the realization of Fusion Energy", plans to develop a technology capable of feeding fusion power into the grid by the 2050, using a demonstration fusion power plant: the EU DEMO. The EUROfusion Roadmap makes it clear that safety is an essential element even in the current pre-conceptual design phase, so this thesis focuses on one of the most representative "Design Basis Accidents" scenarios: an in-vessel Loss of Coolant Accident (LOCA), that has the potential to cause substantial damage to the components inside the vacuum chamber. A LOCA occurs when an unpredicted event causes the failure of the first wall (FW) components, exposing the cooling system, and initiating the release of the coolant inside the vacuum vessel (VV). In the case of a water-cooled breeding blanket (WCLL-BB), the release of high-pressure water inside the low-pressure environment generates a supersonic flashing jet, whose behaviour needs to be addressed. The first section of this work concentrates on the physical study of the flashing phenomenon, analysing the thermodynamical and mechanical processes that characterise the phase change mechanism, and the evolution of the jet after the release, followed by a brief review of the main theoretical models presented in literature. The next step was to examine the predictive capabilities of a CFD model in simulating the multiphase transient that forms in the first milliseconds after the release; this research was carried out in two stages. First, using STAR CCM+, a 2D model was generated to simulate the multiphase phenomenon, confronting the various approaches the code proposes, and selecting the most suitable for the case. The transient was modelled on the basis of an opportune test case chosen from the literature, and was then validated through the comparison with the numerical and experimental results of the case. The model was then modified to match the parameters of the EU DEMO LOCA scenario, and a more case-relevant simulation was carried out. The code demonstrated the capability of simulating such a violent phenomenon, defining the strategy and the models to be adopted in a future full 3D analysis.



# Table of Contents

<b>1</b>	<b>Introduction.....</b>	<b>1</b>
<b>1.1</b>	<b>Background.....</b>	<b>1</b>
<b>1.2</b>	<b>Nuclear fusion.....</b>	<b>2</b>
	<i>1.2.1 Physics basis.....</i>	<i>2</i>
	<i>1.2.2 Fusion reactors.....</i>	<i>4</i>
	<i>1.2.3 Tokamak reactor general functioning.....</i>	<i>5</i>
<b>1.3</b>	<b>EU DEMO Fusion Power Plant.....</b>	<b>7</b>
	<i>1.3.1 Current design baseline.....</i>	<i>7</i>
	<i>1.3.2 Breeding Blanket.....</i>	<i>9</i>
	<i>1.3.3 In-Vessel LOCA.....</i>	<i>10</i>
<b>1.4</b>	<b>Flashing jets.....</b>	<b>10</b>
	<i>1.4.1 Thermodynamic process.....</i>	<i>11</i>
	<i>1.4.2 Nucleation mechanism.....</i>	<i>13</i>
	<i>1.4.3 Under-expanded jet characterization.....</i>	<i>14</i>
	<i>1.4.4 Flashing jet characterization.....</i>	<i>16</i>
<b>1.5</b>	<b>Flashing inception models.....</b>	<b>18</b>
	<i>1.5.1 Nucleation models.....</i>	<i>18</i>
	<i>1.5.2 Bubble growth models.....</i>	<i>20</i>
	<i>1.5.3 Vapor generation models.....</i>	<i>22</i>
<b>1.6</b>	<b>Flashing flows modeling approach.....</b>	<b>23</b>
	<i>1.6.1 Thermal equilibrium.....</i>	<i>23</i>
	<i>1.6.2 Thermal non-equilibrium.....</i>	<i>24</i>
<b>2</b>	<b>Modeling basis.....</b>	<b>26</b>
<b>2.1</b>	<b>Governing equations.....</b>	<b>26</b>

2.1.1	<i>Continuity equation</i>	26
2.1.2	<i>Momentum balance equations</i>	27
2.1.3	<i>Energy Balance equation</i>	29
2.1.4	<i>Equations of state</i>	30
2.1.5	<i>Turbulence</i>	31
<b>2.2</b>	<b>CFD</b>	<b>33</b>
2.2.1	<i>STAR-CCM+</i>	34
2.2.2	<i>Multiphase flows models</i>	35
<b>3</b>	<b>Model development and validation</b>	<b>37</b>
<b>3.1</b>	<b>Publication considered for this work</b>	<b>37</b>
<b>3.2</b>	<b>CFD modeling procedure</b>	<b>38</b>
3.2.1	<i>Geometry</i>	38
3.2.2	<i>Mesh</i>	39
3.2.3	<i>Physics models and solvers</i>	43
3.2.4	<i>Initial conditions</i>	46
3.2.5	<i>Boundary conditions</i>	47
<b>3.3</b>	<b>Model validation</b>	<b>49</b>
<b>4</b>	<b>Model application to an EU DEMO LOCA scenario</b>	<b>53</b>
<b>4.1</b>	<b>General scenario</b>	<b>53</b>
<b>4.2</b>	<b>Model adaptation</b>	<b>53</b>
4.2.1	<i>Geometry and Mesh</i>	53
4.2.2	<i>Boundary/Initial conditions</i>	56
4.2.3	<i>Models and Solvers tuning</i>	57
<b>4.3</b>	<b>Results and discussion</b>	<b>59</b>
4.3.1	<i>Flow development</i>	59
4.3.2	<i>Pressure</i>	63
4.3.3	<i>Temperature</i>	65
4.3.4	<i>Comparison with the HCPB case</i>	67
<b>5</b>	<b>Conclusions</b>	<b>69</b>
	<b>Bibliography</b>	<b>71</b>

# List of Figures

Figure 1-1 – Cross section of fusion reactions for several light elements. Reproduced from [4] .....	3
Figure 1-2 – The EU DEMO tokamak .....	6
Figure 1-3 – p-V stability diagram .....	11
Figure 1-4 – p-T saturation diagram .....	12
Figure 1-5 – Shock diamonds in un under-expanded jet. Reproduced from [14] .....	15
Figure 1-6 – Schematic flashing jet .....	17
Figure 1-7 – Nucleation process model approaches. (I) subcooled liquid; (II) superheated liquid; (III) nucleation (non-equilibrium); (IV) equilibrium .....	18
Figure 2-1 – Regions of the IAPWS-IF97 formulation.....	31
Figure 3-1 – Minato geometry - Case B.....	38
Figure 3-2 – Model geometry - Complete domain (right), pipe and vessel (left) .....	39
Figure 3-3 – Cylinder and Sphere volumetric custom controls .....	41
Figure 3-4 – Mesh adaptation after 1 ms .....	42
Figure 3-5 – Initial water volume fraction .....	47
Figure 3-6 – Boundary conditions - Minato .....	48
Figure 3-7 – Void fraction comparison .....	49
Figure 3-8 – Pressure field comparison .....	50
Figure 3-9 – Water velocity comparison .....	51
Figure 3-10 – Vapor velocity comparison .....	51
Figure 3-11 – Mass flow rate - pipe inlet .....	52
Figure 4-1 – Geometry and dimensions - DEMO.....	54
Figure 4-2 – Custom control volumes, and mesh refinement at 1ms .....	55
Figure 4-3 – DEMO - Initial and boundary conditions .....	56
Figure 4-4 – Mach solution with axial velocity, pressure, and temperature at t=7.9ms .....	60
Figure 4-5 – Shock wave development and coalescence near the pipe outlet, at (a) t=0.88ms, (b) t=1ms, (c) t=1.1ms, (d) t=1.25ms .....	61
Figure 4-6 – Shock impact on opposite wall, at (a) t=10ms, (b) t=13ms, (c) t=16ms .....	61
Figure 4-7 – Velocity vector field at t=18ms .....	62
Figure 4-8 – Pressure distribution, and profile along the axis, at t=19ms .....	63
Figure 4-9 – Void Fraction (left) and Absolute pressure vs Saturation pressure (right) at (a) t=1ms, (b) t=7.9ms, (c) t=17ms .....	64
Figure 4-10 – Pressure evolution on wall opposite to the break.....	65
Figure 4-11 – Temperature distribution, and profile along the axis, at t=19ms .....	66
Figure 4-12 – Near Wall Temperature increase .....	66

# List of Tables

Table 1-1 – DEMO parameters .....	8
Table 1-2 – DEMO design assumptions .....	8
Table 1-3 – DEMO design integration issues .....	9
Table 3-1 – Initial Thermodynamic State - Minato.....	46
Table 4-1 – Initial Thermodynamic State - DEMO .....	57
Table 4-2 – Convective CFL Condition parameters .....	58

# List of Abbreviations

IAEA	International Atomic Energy Agency
ITER	International Thermonuclear Experimental Reactor
DEMO	Demonstration Fusion Power Plant
TF	Toroidal Field
PF	Poloidal Field
DIV	Divertor
FW	First Wall
BB	Breeding Blanket
VV	Vacuum Vessel
CRY	Cryostat
HCPB	Helium Cooled Pebble Bed
WCLL	Water Cooled Lithium Lead
SMS	Singular Module Segment
PWR	Pressurised Water Reactor
DWT	Double-Wall Tubes
LOCA	Loss Of Coolant Accident
CFD	Computational Fluid Dynamics
PDF	Probability Density Function
HRM	Homogeneous Relaxation Model
HEM	Homogeneous Equilibrium Model
IAPWS-IF97	International Association for the Properties of Water and Steam – Industrial Formulation 1997
DNS	Direct Numerical Simulation
LES	Large Eddy Simulation
RANS	Raynolds-Averaged Navier-Stokes
TVH	Turbulent Viscosity Hypothesis
FD	Finite Differences
FV	Finite Volumes
CAE	Computer Aided Engineering
CAD	Computer Aided Design
EMP	Eulerian Multi-Phase
MMP	Mixture Multi-Phase
VOF	Volume Of Fluid
LMP	Lagrangian Multi-Phase
DMP	Dispersed Multi-Phase
CFT	Critical Flow Test
CFL	Courant-Friedrichs-Lax
SIMPLE	Semi-Implicit Pressure-Linked Equation
URF	Under-Relaxation Factor
AMG	Algebraic Multi-Grid
HIRC	High-Resolution Interface Capturing

# List of Symbols

<b>Chemical elements</b>		
H		Hydrogen
D		Deuterium
T		Tritium
He		Helium
Li		Lithium
Pb		Lead
<b>Physical quantities</b>		
$t$	$s$	Time
$m$	$kg$	Mass
$l$	$m$	Length
$D$	$m$	Inlet diameter
$S$	$m^2$	Surface
$V$	$m^3$	Volume
$p$	$bar$	Pressure
$T$	$K$	Temperature
$\rho$	$kg/m^3$	Density
$E$	$J$	Total energy
$e$	$J$	Internal energy
$h$	$J/kg$	Enthalpy
$L$	$J$	Work
$q$	$J/m^2 s$	Heat flux
$\mu$	$Pa \cdot s$	Dynamic viscosity
$\lambda$	$Pa \cdot s$	Bulk viscosity
$\mathcal{M}$	$kg/mol$	Molecular weight
$R$	$J/kg K$	Gas specific constant
$c_p$	$J/kg K$	Specific heat at constant pressure
$\gamma$		Specific heat ratio
$a$	$m/s$	Velocity of sound
$W$	$m/s$	Shock propagation velocity
$\mathbf{V}$	$m/s$	Velocity vector
$u, v, w$	$m/s$	Velocity cartesian components
$\langle U_i \rangle$	$m/s$	Mean velocity component
$u'_i$	$m/s$	Fluctuating velocity component
$\langle u'_i u'_j \rangle$	$Pa$	Reynold stress tensor
$\bar{\tau}$	$Pa$	Viscous stress tensor
$\mathbf{f}$	$N/kg$	Volume force per mass unit vector

$\dot{q}$	$J/m^2 s$	Conduction heat flux vector
$\xi$	$J/kg s$	Heat absorbed per mass and time unit
$\tau_E$	$s$	Energy confinement time
$N$	$m^{-3}$	Particle number density
$\sigma_p$	$m$	Particle diameter
$J$	$m^{-3}s^{-1}$	Rate of nucleation
$\sigma$	$J/m^2$	Surface tension
$\Delta\mu$	$J/kg$	Chemical potential difference
$\Delta G$	$J$	Gibbs free energy barrier to nucleation
$\eta$		Expansion ratio
$d_b$	$m$	Bubble diameter
$R_b$	$m$	Bubble radius
$N_b$	$m^{-3}$	Bubble number density
$\alpha$		Void fraction
$\chi$		Phase volume fraction
$\varphi$		Heterogeneity factor
$B'$	$s^{-1}$	Rate of molecular interaction
$\Gamma$	$kg/m^3 s$	Vapor generation rate
$\Theta$	$s$	Relaxation time
$S$		Slip-ratio
$\nu_T$	$m^2/s$	Turbulent viscosity
$k$	$m^2/s^2$	Turbulent kinetic energy
$\varepsilon$	$m^2/s^3$	Turbulent dissipation rate
$\delta_c$	$m$	Cell dimension
$\Delta t$	$s$	Time-step
<b>Universal constants</b>		
$k_B$	$1.3806 \cdot 10^{-23}$	$J/K$ Boltzmann constant
$\mathcal{R}$	8.3145	$J/mol K$ Gas universal constant
<b>Dimensionless Numbers</b>		
$Re$	$\rho u D / \mu$	Reynolds Number
$Gb$	$d_{cr} \varphi / k_B T$	Gibbs Number
$Kn$	$k_B T / \sqrt{2} \pi \sigma_p^2 p L$	Knudsen Number

# Chapter 1

## 1 Introduction

### 1.1 Background

The global demand for electricity has grown exponentially in the last decades, and is expected to grow further, reaching the 10 TW mark in the second half of this century [1]. To date, renewable energy sources contribute just over a third of the world's overall electricity production, alone covering three quarters of the new global energy capacity [2], however these production methods are affected by the inconsistency and seasonal variability of the primary sources (i.e., wind, sun). Furthermore, the increasing cost of fossil fuels, and the heightened awareness of the anthropogenic effect on global warming, calls for a new, reliable, sustainable, low-carbon, electricity source: nuclear fusion is regarded as one of the best candidates.

The concept of a controlled nuclear fusion reaction was revealed to the world for the first time in the 1958, during the Second United Nations Conference on the Peaceful Uses of Atomic Energy, held in Geneva. During this event, the Nations involved realized that, in order to develop the theoretical basis and the technology needed to achieve the goal of harnessing this resource for electricity production, a global cooperation was necessary; this marked the beginning of the International Atomic Energy Agency's (IAEA) commitment to the development of the nuclear fusion [3].

Today, Europe efforts to advance nuclear fusion research are coordinated by the EUROfusion Consortium, who superseded the European Fusion Development Agreement (EFDA) in 2013. The goal is to develop a technology capable of feeding fusion electricity into the grid by the 2050, and to achieve this goal, the Consortium drafted the *European Research Roadmap to the Realization of Fusion Energy* [1].

The strategy described in this document can be summarized into three main points:

1. The design and construction of the tokamak ITER (International Thermonuclear Experimental Reactor), which will demonstrate the feasibility of extracting energy from fusion through a technical demonstration: producing 500 MW for 400 seconds.
2. Using to the information acquired from ITER development, another reactor will be design, the DEMO (Demonstration Fusion Power Plant) whose purpose will be to feed into the electric grid hundreds of MW for several hours, operating with a closed fuel cycle.
3. Parallel to the first two points, a great deal of effort will be employed on the scientific research and engineering development of the technologies needed for the transition from the demonstration plants to the large-scale production of fusion plants.

## 1.2 Nuclear fusion

### 1.2.1 *Physics basis*

The nuclear fusion is the reaction that fuels the stars, producing both the heat and the light that reaches us. The principle of the phenomenon is that, when two atomic nuclei collide with enough energy, they fuse together, generating a heavier nucleus, and subatomic particles (neutrons or protons). The difference between the combined mass of the colliding nuclei and the mass of the generated nucleus, define the type of reaction: less mass in the products means that energy is released (exothermal reaction), more mass in the product means that energy is absorbed (endothermal reaction). Reaction between nuclei lighter than iron-56 or nickel-62 are exothermal, and are in fact the kind of reaction that take place in stars core.

Atomic nuclei are naturally prone to repel each other, due the fact that the positively charged protons inside them are subject to a repulsive electrostatic force. However, if the two nuclei are brought close enough together, overcoming a certain energy barrier (the Coulomb barrier), another force takes over: the *nuclear force* (historically: strong nuclear force) that act between the nucleons (subatomic particles inside the atomic nucleus, i.e., neutrons and protons), and that allows the combination of the two nuclei into a heavier one. The nuclear force is a short-range force, meaning that, inside a nucleus, nucleons are attracted only by the neighbours; on the other hand, the repulsive electrostatic force between protons is an inverse square force, meaning that all the protons inside the nucleus repel each other. The net sum of these forces acting on a single nucleon is defined *binding energy*, and

increases with the size of the nucleus, up to iron and nickel, and then decreases as the nucleus becomes heavier. Isotopes with more neutrons inside the nucleus, have a higher binding energy, and consequently a lower Coulomb energy barrier.

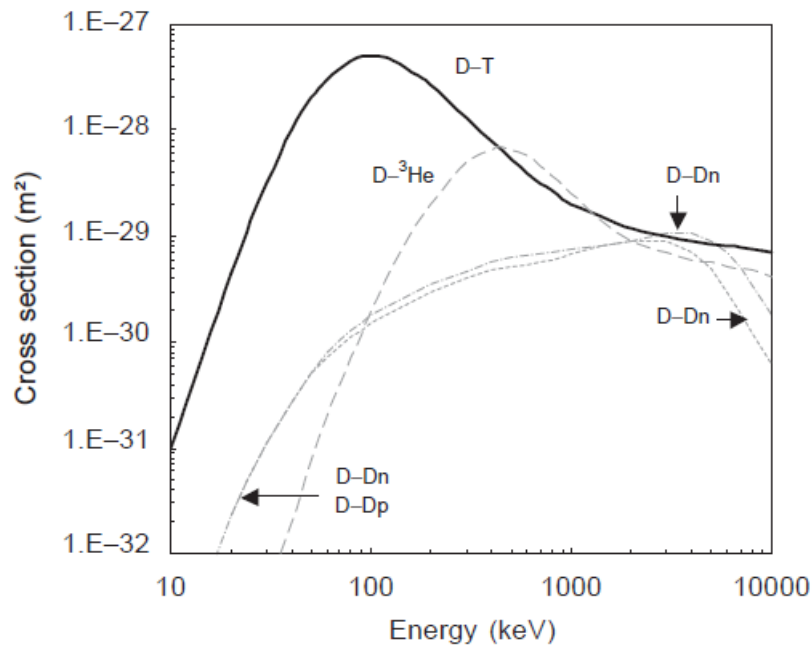


Figure 1-1 – Cross section of fusion reactions for several light elements.  
Reproduced from [4]

To obtain a fusion reaction, and overcome the Coulomb barrier, a certain amount of energy is needed: the probability of crossing this barrier, as a function of the relative velocity of the two nuclei is called *cross section*. If one considers several fusion reactions, this function can be averaged over the distribution of velocities (e.g., thermal distribution).

Figure 1-1 provides a representation of the cross section of several fusion reaction as a function of interaction energy. As it can be seen, the energy required to start a fusion reaction is at least in the order of 10 keV, which corresponds to more than 10 million Kelvin; at this temperature the matter is in plasma form, a state where the electrons are stripped from the atom nucleus. As shown in the graphic, the reaction that requires the least amount of interaction energy is the fusion between two isotopes of hydrogen, deuterium (D or  $^2\text{H}$ ) and tritium (T or  $^3\text{H}$ ), which is in fact the best candidate to controlled fusion inside a reactor.

### 1.2.2 Fusion reactors

As said, the best candidate reaction for a controlled fusion inside a reactor is the D-T:



when the nuclei of D and T collides, they fuse to form a nucleus of helium (alpha particle) and a neutron, with a surplus of energy, in the form of kinetic energy of the product particles. In order to have a continuous reaction, the energy generated must be enough to compensate for the losses, and to sustain new reactions inside the plasma. This concept is described by the *Lawson criterion* [4], which compares the energy produced by a fusion reaction, with the energy losses to the environment:

$$N \cdot \tau_E > g(T) \cdot f(Q) \quad (1.2)$$

$\tau_E$  is the *energy confinement time*, is defined as the time required for the plasma to completely lose all its energy if fusion reactions suddenly stop;  $N$  is the particle number density;  $g(T)$  is the reaction rate in function of the temperature, and  $Q$  is the relation between the power generated by the fusion, and the power fed to the plasma from the outside;  $Q = 1$  means that the power generated and the power provided are equivalent, while the ideal condition is reached when  $Q = \infty$ , which means that no energy is supplied from the outside, and the reaction is said to be “in ignition”. Based on Lawson criterion, two different approaches can be followed:

1. Inertial confinement: a small quantity of fuel (small  $n$ ) is subjected to high temperature and high pressure for a very small time ( $\tau_E \approx 10^{-12}$  s).
2. Magnetic confinement: the plasma is heated to a very high temperature and confined inside a magnetic field, for a time on the order of a few seconds, allowing for a continual reaction. This method is better suited for energy production applications; the DEMO project uses this approach.

#### 1.2.2.1 Magnetic confinement

Plasma is the fourth state of matter, where the high level of thermal agitation separates the electrons from their atomic nuclei, creating a globally neutral ionized gas, in which electrically charged particles flow free. This fluid cannot be confined through conventional means, being that no known material can withstand such high temperatures (i.e., 10 million degree); the only way possible is to use a magnetic field. Various shape of magnetic fields has been studied, and to date the best configuration is the toric one, where charged particle follows field lines closed on themselves, drawing helical trajectories. The toroidal field (TF) configuration however is characterized by a drift of

electrons and ions, where differently charged particles tend to separate. To address the problem is necessary to modify the field lines, making them helicoidal rather than straight (circular), by means of a second magnetic field; the method by which this second magnetic field is generated, defines another distinction:

1. In a *tokamak* type reactor is the plasma itself that creates the second magnetic field, the “poloidal field”, perpendicular to the toroidal. The efforts of the EUROfusion Consortium are oriented toward the development of a reactor with this configuration.
2. In a *stellarator* type reactor, all the magnetic fields that hold the plasma are generated through external electromagnets. This second configuration is technically more complicated, so its development is lagging behind of the tokamak one, but it’s still studied because it features some interesting qualities.

### 1.2.3 Tokamak reactor general functioning

The name “tokamak” is an acronym from the Russian “*тороидальная камера магнитными катушками*”, which translates as “toroidal chamber with magnetic coils”. Inside the *Plasma Chamber* the fuel (i.e., deuterium and tritium) is injected in the form of frozen pellets or gas. Here the fuel is heated by means of beams of high-energy neutral particles, or by electromagnetic waves at a certain characteristic frequency. The now heated plasma is confined by the magnetic field, and further heated by the current circulating in the plasma itself (Joule effect). When the reaction reaches a value of  $Q = 5$ , the main heating source is provided by the highly energetic helium nuclei formed during the fusion that remains trapped inside the plasma. To prevent the concentration of helium nuclei from reaching values that compromise the fusion reaction, the *Divertor*, a specific device placed at the bottom of the chamber, uses a poloidal magnetic surface to attract and then extract the unwanted particles. All the surfaces that face the plasma are exposed to neutronic, thermal, radiative, and thermomechanical stress loads, thus their management is critical. [4] Behind the so called “first wall” (FW), is located the *Breeding Blanket* (BB), that performs two main tasks: it shields the outer components from the neutron and gamma radiations, by means of an internal circulating coolant (helium or water [5]), and uses the kinetic energy of neutrons (80% of the total energy for D-T plasma) to produce tritium from lithium through two reactions [4]:



The first reaction (1.3) is exothermic, thus is preferable. In the breeding blanket the lithium can be in liquid (metallic alloy) or solid (ceramic) form, and represent the second consumed fuel inside the fusion reactor. However, the reaction (1.1) produces only one neutron, and the reactions (1.3) and (1.4) produce only one atom of tritium; considering the inevitable neutron losses, the tritium production needs to be enhanced by a neutron multiplier: for this purpose, metals such as lead or beryllium are introduced into the blanket. The toroidal chamber, the first wall and the breeding blanket are all contained inside the *Vacuum Vessel* (VV), a hermetically sealed steel container that encloses the space where fusion reaction takes place, and act as a first safety barrier against radioactivity. The vacuum vessel is in turn contained inside a larger structure, the *Cryostat*, a high-vacuum pressure chamber that provides the ultra-cool environment needed by the superconducting magnets. [6] The heat generated in the neutron breeding process, as well as during the fusion reaction and on the surfaces of the divertor is extracted by a coolant that flows inside the vacuum vessel walls, that is then used to generate steam and, through a conventional turbine and alternator, to produce electricity.

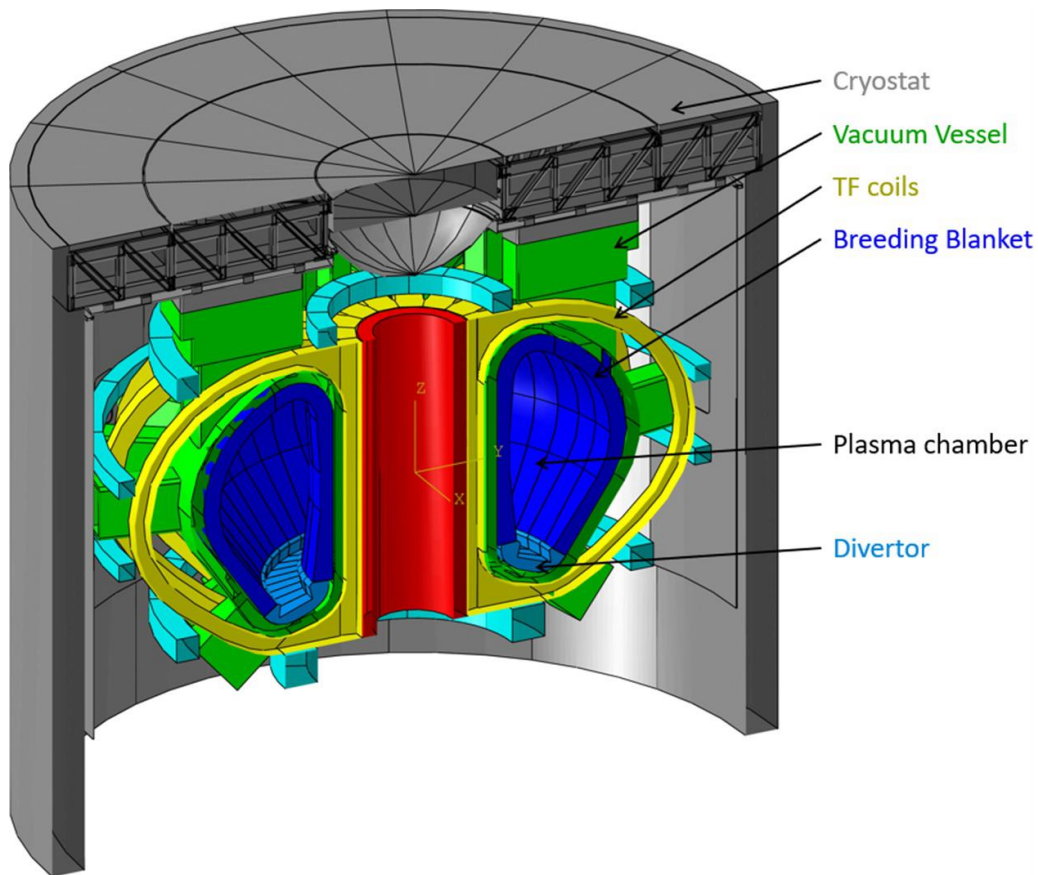


Figure 1-2 – The EU DEMO tokamak

## 1.3 EU DEMO Fusion Power Plant

The fusion power plants currently in development (i.e., ITER) aim to investigate plasma physics, and to demonstrate the feasibility of extracting energy from fusion. The construction of the DEMO will demonstrate the capability of a fusion plant to produce electricity for commercial purposes, with the central requirement to feed into the power grid 300÷500 of MW for several hours, operating with a closed tritium cycle. The DEMO development strategy must consider technological and engineering limitations, paying particular attention to the safety and reliability of the plant, as well as to operational aspects, such as maintenance. To meet all these requirements, the design approach includes some key features:

1. a design philosophy that aims to develop individual systems in the context of a wider integrated system concept.
2. the use of technologies and knowledge acquired during the design and development of ITER.
3. the parallel study of multiple design options for new systems and technologies with high risk factors.

### 1.3.1 *Current design baseline*

To date, the final design of DEMO has not yet been formally selected, but its development proceeds in parallel with the construction of ITER, with a final conceptual design that, according to the ambitions of the EUROfusion Roadmap, will be ready by the 2027.

The parameters that drive the design of DEMO are defined by the high-level requirements that the plant must achieve (e.g., net power output, tritium self-sufficiency, etc.) and are limited by the current availability of technologies, and technical risk associated with the various design option. Figure 1-2 shows the CAD of the EU DEMO tokamak, highlighting the main components. Table 1-1 lists the parameters of the current DEMO design, while Table 1-2 presents the main design assumptions. There are also several integration issues that have a strong impact on the DEMO architecture that have yet to be resolved Table 1-3. [7]

Table 1-1 – DEMO parameters

<b>Characteristics</b>	
Aspect ratio	3.1
Major/minor radius (m)	9.0/2.9
Plasma current (MA)	18.0
Elongation/triangularity (95%)	1.59/0.33
Toroidal field, axis/coil-peak (T)	5.9/>12.5
Auxiliary heating power – flat top (MW)	50
<b>Performances</b>	
Fusion Power (MW)	2000
Electric output (MW)	500
Neutron wall loading (MW/m <sup>2</sup> )	1.04
Burn time (s)	7200
Dwell time (s)	<600
Volt-sec capability/Volt-sec for burn (Vs)	728/365
Loop voltage (V)	0.048
$\beta_{n,tot}$	2.5%
Av. electron temperature (keV)	12.6
Av. electron density/Greenwald density limit (10 <sup>20</sup> m <sup>-3</sup> )	0.73/0.67
$Z_{eff}$	2.2
Plasma stored energy (GJ)	1.181
Divertor Challenge quantifier $P_{sep}B/qAR$ (MWT/m)	9.2

Table 1-2 – DEMO design assumptions

Single-null water cooled divertor; PFC armour: W
Low Temperature Super Conducting magnets Nb <sub>3</sub> Sn
16 TF coils; B <sub>max</sub> conductor ~ 12 T
EUROFER for IVCs, AISI ITER-grade 316 for VV
In-vessel RH: vertical (blanket) / horizontal (divertor)
DEMO plant lifetime ~ 7-8 fpy
Neutron wall loading ~ 1MW/m <sup>2</sup>
Thermal conversion efficiency > 30%
Tritium fuel cycle: self sufficient
Blanket lifetime
- starter blanket: 20 dpa
- second blanket: 50 dpa

*Table 1-3 – DEMO design integration issues*

- 
- Performance of wall protection limiters during plasma transients
  - Integrated design of breeding blanket and ancillary systems
  - Engineering of risks arising from magnetic divertor configuration
  - Design of breeding blanket vertical segment architecture
  - Design of Power Conversion System Options (i.e., direct or indirect)
  - Design of tokamak building concept and ex-VV maintenance
  - Design of tritium direct recirculating pumping concept
  - Development of a reliable plasma-operating scenario
- 

### *1.3.2 Breeding Blanket*

As showed in Table 1-3, the design of the breeding blanket, and in particular the choice of the coolant, is one of the main issues that affects the general architecture of the nuclear plant, as it goes to interact with all other systems, thus presenting integration problems, as well as safety concerns. In fact, the function that a breeding blanket must perform within the DEMO are numerous [5]:

- It must absorb the energy of the neutron bombardment, which makes up about 80% of the total plasma energy. In a reactor in the power order of 2GW, this energy adds up to about 1900 MW. To extract and convert this energy, the chosen cooling needs an adequate thermodynamic efficiency, so it must be at high pressures and temperatures.
- It must be able to reliably breed the tritium (see Section 1.2.3).
- It must contribute to effectively shield from neutron and gamma radiation all the elements outside the vacuum vessel.

The heat extraction and the radiation shielding are the requirements that most affect the choice of the coolant, that in fact is still open. Two main BB concepts are now being investigated: the HCPB (Helium-Cooled Pebble Bed) and the WCLL (Water-Cooled Lithium-Lead); the model DEMO plant of interest for this work is based on the latter.

#### *1.3.2.1 Water-Cooled Lithium-Lead Breeding Blanket (WCLL-BB)*

The current design of the DEMO WCLL-BB is characterized by a modular approach (SMS – Singular Module Segment), and is in fact divided into 16 sectors, one for each TF coil. The structural material is a reduced activation ferritic-martensitic steel, the EUROFER97, and the breeding and neutron multiplier material is a Lithium-Lead alloy (Pb-Li). The coolant is water at Pressurized Water Reactor (PWR) conditions: nominal pressure of 15.5 MPa and a temperature of 295-328°C. To improve the reliability of the blanket, it

was decided to adopt two independent cooling systems, respectively in the first wall, and in the breeding zone. The first wall plasma facing surface is covered by a 2mm thick tungsten layer, cooled by a system of square channels (7 x 7 mm) inside which water flows in a counter-current direction. The breeding zone cooling system extract heat from the structure and from the breeding material, using a Double-Wall Tubes (DWT) technology, in order to reduce the reaction risk between the water and the Pb-Li. [5] [8]

### 1.3.3 *In-Vessel LOCA*

Mission 5 described in the EUROfusion Roadmap makes it clear that safety is an essential element in the EU DEMO design phase. The plan anticipates the need to identify the accident scenarios that can affect the plant or potentially harm the personnel, and to focus on avoiding the initiating events. This can be done by design (“passive safety”), or by monitoring the state of the plant and components (“defence in depth”). [1]

The in-Vessel Loss-Of-Coolant Accident has been classified among the most representative “Design Basis Accidents” scenarios, because it has the potential to cause substantial damage to the components in the VV. It occurs when an uncontrolled energy transfer from the plasma to the FW causes an increase of the wall temperature, up to the material (EUROFER97) limit, causing the failure of the component. When this happens, a certain number of cooling system channel are exposed, releasing the pressurized coolant into the reaction chamber. [9]

If this occurs, the coolant generates a supersonic flash boiling jet, where, due to the remarkable pressure differential, the water instantly evaporates into steam. This work aims to define a computational model capable of simulating the physics of such a scenario, and its effects on the integrity of the vacuum vessel.

## 1.4 **Flashing jets**

As said in Section 1.3.2, the coolant used inside the breeding blanket is water at Pressurized Water Reactor (PWR) conditions: a pressure of 15.5 MPa (155 bar), and a temperature of 295 – 328°C (568.15 – 601.15 K). Since the saturation temperature of water at that pressure (344.8°C) is higher than the actual operating temperature, the water is in what is defined as *subcooled* state, that is a stable condition. In the event of a LOCA, the water would accidentally be released inside an environment with a very low pressure (10 kPa): the great difference between the internal and external pressure causes the explosive generation of vapor (flashing), and the formation of a two-phase

jet. However, the behaviour of a two-phase flashing jet is complicated, so in order to understand all its characteristics, is useful to focus on one process at a time.

### 1.4.1 Thermodynamic process

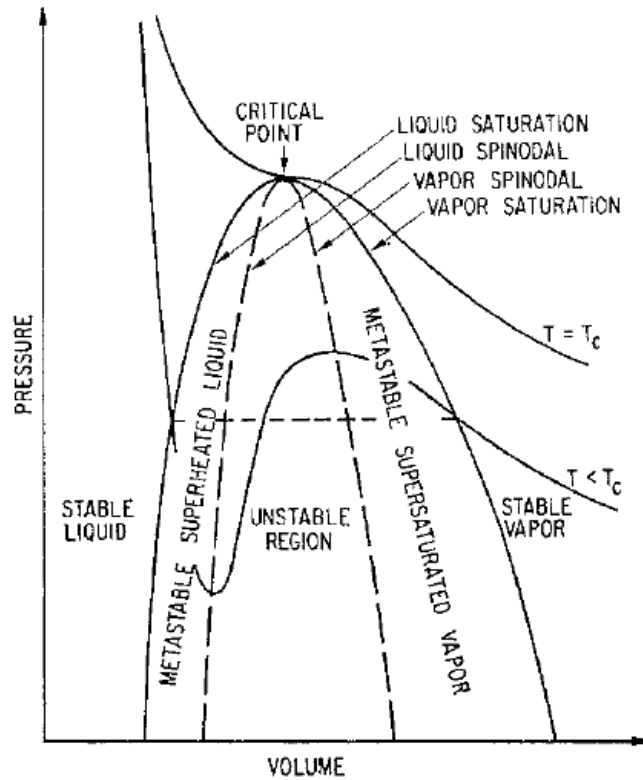


Figure 1-3 – p-V stability diagram

Figure 1-3 shows the characteristic pressure-volume diagram for a fluid. The two descending lines are the isothermal Van der Waals equation of state (1.4), calculated for two temperature values: the critical temperature  $T_c$ , and a generic  $T < T_c$ . For a given pressure, the solution identifies three volume values: the smallest value identifies the condition of saturated liquid, the largest value the condition of saturated vapor, while the middle value does not have a physical meaning. Each isothermal curve also has a maximum and a minimum, defined as spinodal points.

$$\left(P + \frac{an^2}{V^2}\right)(V - nb) = nRT \quad (1.5)$$

The stability diagram is obtained by joining these characteristic points defined for each isothermal curve. The diagram presents five regions: a *stable liquid region* on the left, and a *stable vapor region* on the right, in the middle is what is called the *saturation dome*, in turn divided by the spinodal curve into the metastable *superheated liquid region*, the metastable *supersaturated vapor region*, and the unstable region.

A subcooled liquid is located in the region of stable liquid, but it can gain the superheated condition in two way: it can be isothermally depressurized, so its condition moves down the Van der Waals curve (Figure 1-4, A), or it can be isobaric heated, meaning it moves horizontally on the stability diagram (Figure 1-4, B). When in the superheated condition, if the decompression (or heating) process keeps going, the liquid will eventually reach the thermodynamic limit of absolutely instable state, the spinodal curve, beyond which any perturbation of the fluid will cause irreversible reaction that will lead to the generation of vapor.

The phase change due to depressurization can be different, depending on the initial conditions. If the fluid is at relatively low temperature and pressure, occurs what is called “cavitation”, where a small superheat is enough to initiate the phase change. Bubble formation and growth is mainly driven by mechanical non-equilibrium processes across bubble interfaces, and thermal effects are negligible. If the fluid is at high temperature or pressure, the phase change takes place through “flashing”, a phenomenon characterized by high thermal non equilibrium, where the vaporization is limited by the heat transfer rate between phases. [10]

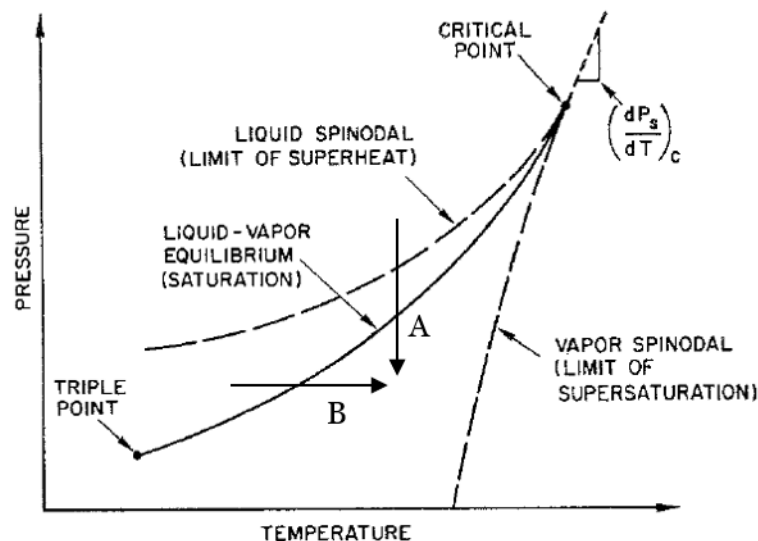


Figure 1-4 – p-T saturation diagram

## 1.4.2 Nucleation mechanism

Nucleation is the mechanism by which phase change begins within the liquid. To understand how this happens, is necessary the knowledge of three fundamental processes: the thermodynamics of phase change, the dynamic of bubble growth and the probability of existence of molecular clusters within a liquid. According to the thermodynamic theory, the flashing occurs once the liquid reaches the thermodynamic limit of superheat, i.e., the spinodal curve, defined as the minimum point in the liquid isothermal curve, which satisfies the conditions  $(\partial p/\partial V)_T = 0$ , and  $(\partial^2 p/\partial V^2)_T > 0$ . This situation never verifies, as experiments show that the phase change always takes place before that point, so another two empirical kinetic limits has been defined: the *homogeneous nucleation limit* and the *heterogeneous nucleation limit*.

### 1.4.2.1 Homogeneous nucleation

The homogeneous nucleation process occurs in absence of pre-existing seeding points inside the liquid, and is considered a fundamental mechanism of first-order phase transition. The process accounts for the molecules that possess enough energy to overcome the free energy barrier and carry out the phase transition, and the rate of nucleation is expressed by the following relation:

$$J = A \exp(-\Delta G/k_B T) \quad (1.6)$$

$$A = N(-3\sigma/\pi m) \quad (1.7)$$

$$\Delta G = 16\pi\sigma^3/3\Delta\mu^2 \quad (1.8)$$

The pre-exponential factor  $A$  has a kinetic connotation, and is calculated through the number density of the molecules inside the superheated fluid ( $N$ ) and the surface tension ( $\sigma$ ), while the exponent accounts for the thermodynamic effects through the definition of the free energy barrier to nucleation ( $\Delta G$ ), and the Boltzmann's constant ( $k_B$ ). [11]

### 1.4.2.2 Heterogeneous nucleation

The heterogeneous nucleation is a second-order phase transition, where the beginning of the phase change is assisted by the presence of impurities inside the liquid, like dust particles, dissolved gases, or wall roughness. In correspondence with these sites, the surface energy is lower, thus reducing the free energy barrier, and facilitating nucleation. [11]

It is found that when a subcooled liquid undergoes a rapid adiabatic depressurization (pulse expansion) it may reach the homogeneous nucleation limit of superheat before experimenting a phase transition. In order to remain in equilibrium during the depressurization, the liquid needs to lose internal

energy, and this is achieved through the release of the latent heat of vaporization, sparked by the bubble formation through the fluctuations of the molecular thermal agitation velocity. The bubbles formation and growth then increase the vapor content inside the liquid, until a certain limit is reached, where the pressure recovery rate due to the vapor generation equals the depressurization rate imposed on the liquid before the flashing: this point is defined as *flashing inception*. [12]

### 1.4.3 Under-expanded jet characterization

In general, the behaviour of a gaseous jet is determined by the level of under-expansion, that is the ratio of the exit pressure (i.e., the pressure at the nozzle exit), and the ambient pressure:

$$\eta = p_{exit}/p_{amb} \quad (1.9)$$

For a not under-expanded ( $\eta = 1$ ) single-phase steady jet, the characterization can be carried out through the study of the centreline velocity profiles. Near the nozzle there is a conical region, the *potential core*, where the velocity is constant and equal to the exit velocity. The extent of this region ( $\sim 4\div 6$  nozzle diameters) is determined by the presence of the shear layer that is formed at the boundary of the jet, where it meets the stationary fluid of the environment. Where the growing boundary layer converges on the jet axis, begins what is called the *transition region*. Here is where the mixing of the flow takes place, which begins to exhibit turbulent characteristics, and where the centreline velocity begins to decay. Further downstream the velocity profiles take on a Gaussian shape, and if properly dimensioned, become self-similar. The interaction of the jet with the environment involves the exchange of mass, momentum, and energy. It is interesting to note that the momentum of the entrained mass compensates for the losses generated by the jet propagation, thus the momentum is constant along the jet axis. [11]

For an under-expanded ( $\eta > 1$ ) single-phase jet, the level of under expansion have a significant impact on the behaviour of the flow, and it may be important also for the study of the under-expanded flashing jets. In general, this situation occurs when the pressure at the nozzle exit is higher than the ambient pressure, and it implies the presence of a choking condition, meaning that the flow inside the nozzle accelerates until it becomes sonic, and no information can travel back inside the nozzle. When the flow reaches the break plane with a pressure higher than the ambient pressure, it tries to equalize it by expanding; while the flow near the centreline keeps moving forward, the flow near the nozzle edge begins to turn outward, generating a fan of isentropic expansion waves, the so called Prandtl Meyer expansion mechanism, that lowers the pressure. The expansion waves, pointed inward, meets on the centreline, where are reflected back outward, toward the free jet boundary. Here they intersect the slip line that separates



#### 1.4.4 *Flashing jet characterization*

A flashing, two-phase jet is expected to behave differently from a gaseous single-phase jet; its behaviour is furthermore expected to be far more complex, and it heavily depends on the condition of the fluid before the flashing, such as the degree of superheat, the level of under-expansion, the pressure, the presence of impurities, and even the internal roughness of the nozzle. Depending on the initial conditions, the flashing can occur inside the nozzle, thus the jet emerges as an unstable flow of large, superheated liquid droplets, that then start to break up and evaporate, giving the jet an explosive characteristic, or it can occur at the exit region, and the behaviour is dominated by the surface evaporation. [11] Even the relationship between under-expansion and choking is different compared to the single-phase case: a flashing jet can be under-expanded if the vaporization is fast enough to maintain the exit pressure above the ambient level, whether the flow is choked or not. [13]

A general approach in the determination of a flashing jet characteristic is to differentiate between the mechanical and the thermal effects. [15]

##### 1.4.4.1 *Mechanical effects*

The parameter that best describes the mechanical properties of the flow is the Reynolds number, function of the exit velocity ( $u$ ), the nozzle outlet diameter ( $D$ ), the viscosity ( $\mu$ ), and the density of the fluid ( $\rho$ ):

$$Re = \rho u D / \mu \quad (1.10)$$

For high values of expansion rate, that is, the ratio between tank and ambient pressure, the Reynolds number increases, with a consequent transition to the turbulent regime. If the Reynolds number is sufficiently high, the transition may happen inside the nozzle (Figure 1-6, c), in the liquid part of the flow, and this may lead to a certain kind of scenarios: the perturbation inside the flow may be amplified, causing an increase in the break-up mechanisms, and consequently the formation of more droplets and liquid ligaments at the nozzle outlet (Figure 1-6, d). Higher Reynolds number also means higher exit velocity, with a consequent increase of the entrainment, and a stronger mixing of the droplets inside the jet. Here the turbulence plays another role, promoting the formation of smaller droplets on the liquid surface through the turbulent eddies inside the flow, or by the Kelvin-Helmholtz and Rayleigh-Taylor instabilities on the liquid surface (Figure 1-6, e). [16] Another process that could intervene in the bubble formation inside the flow is cavitation, whose mechanism, in the simplest models, is described as driven only by mechanical effects, such the pressure difference between the vapor and the liquid. [17]

#### 1.4.4.2 Thermal effects

The main thermodynamic processes that govern the phase change during flashing are evaporation and boiling, and their development inside the flow depends mostly on the rate of heat transfer by conduction, as well as on the presence of impurities, and obviously on the thermodynamic conditions of the fluid (i.e., temperature, pressure). Evaporation occurs when the molecules have enough kinetic energy to escape from the liquid into the vapor phase, hence it is a superficial phenomenon. As the liquid temperature increases, the vapor pressure reaches the ambient pressure, and vapor bubbles start to form inside the liquid: this is the boiling process, which is a volume phenomenon. The boiling process may also favour the droplet formation on the liquid surface due to the rapid growth of the vapor bubbles within the jet. The degree of superheat plays an important role on the balance of the two phenomena: a fluid with a low degree of superheat is mostly governed by evaporation, hence the flashing occurs late, and a liquid core forms inside the jet. When the degree of superheat raises, boiling is the prevailing thermal mechanism, with a rapid break-up of the fluid in large droplets inside the nozzle, and an explosive evaporation of the smaller droplets outside of it.

Figure 1-6 summarizes the general aspects that characterize a flashing jet: (a) identifies the general condition inside the tank, that is, total pressure, total temperature, degree of superheat, initial turbulence level, liquid density, viscosity, etc.; (b) represents the influence of the nozzle, such as its shape, length, and surface roughness; (c) is the section inside the nozzle where all the flow break-up mechanisms previously described takes place: boiling, cavitation, turbulent droplet formation. Here is where the two-phase flow pattern is determined; (d) is the region where the entrainment of the external air increases the turbulence level, and together with the boiling helps the formation of smaller droplets; (e) by this section the liquid have completely been nebulized into small droplet, and the only ongoing thermal process is evaporation.

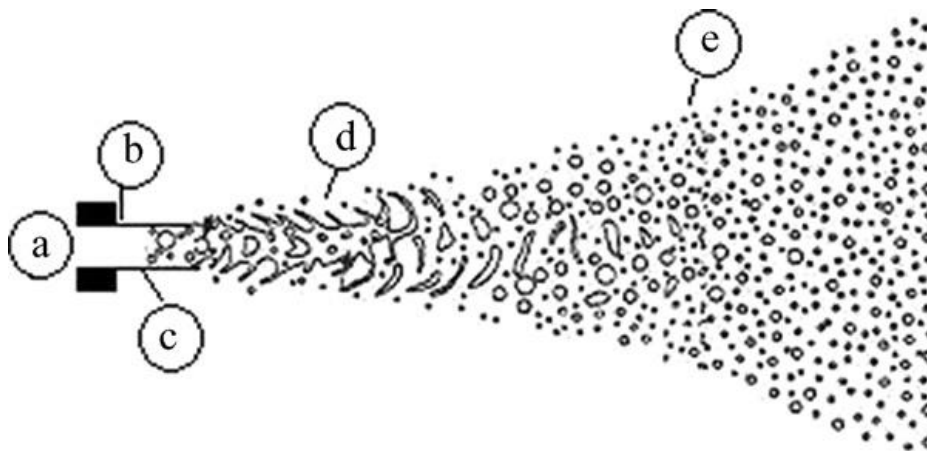


Figure 1-6 – Schematic flashing jet

## 1.5 Flashing inception models

The creation of a physical model that faithfully describe the behaviour of a two-phase flow with mass and heat transfer present a lot of challenges. One of the many issues is to model the mechanisms that trigger the flashing inception inside the fluid. In literature the main models described are the processes of vapor bubble formation, the bubble growth, and the method of vapor generation.

### 1.5.1 Nucleation models

To date is not possible to simulate the formation of the bubbles inside the flow, so the common approach is to estimate the information through analytical means and then impose it as a boundary condition in the CFD simulation. This process can be implemented by three main methods: the homogeneous “seeding”, a “step” function, or the “nucleation” model. [10]

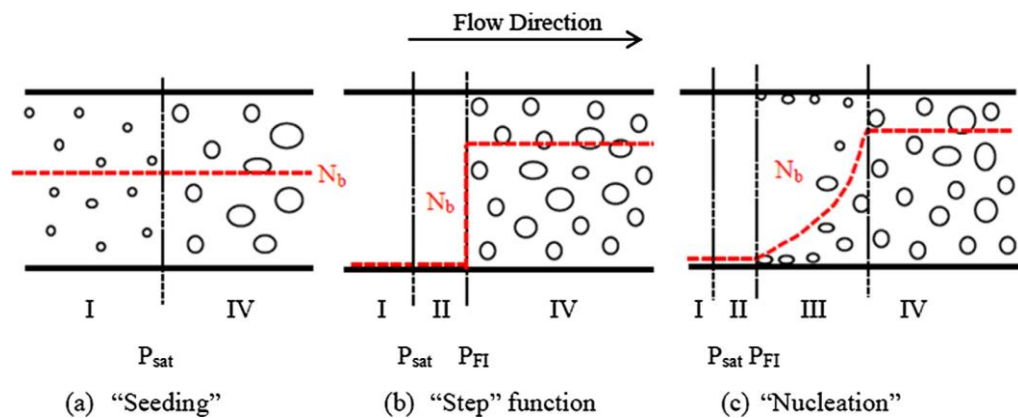


Figure 1-7 – Nucleation process model approaches. (I) subcooled liquid; (II) superheated liquid; (III) nucleation (non-equilibrium); (IV) equilibrium

#### 1.5.1.1 Homogeneous seeding

In this model it is assumed that a number of small vapor bubbles are already present in the subcooled liquid. When the liquid reaches the superheat condition, these bubbles will start to grow, with a bubble diameter increasing according to the relation:

$$d_b = \left( \frac{6\alpha}{\pi N_b} \right)^{1/3} \quad (1.11)$$

where  $\alpha$  is the vapor volume fraction, and  $N_b$  is the number density of bubbles.

The method strongly depends on these two parameters, that therefore must be defined in advance. Various authors have proposed different values for the bubble concentration  $N_b$ , depending on the model configuration, and have found that it is strongly affected by the initial temperature of the liquid. The major advantage of this method is that the bubble growth is directly correlated with the increase of the vapour fraction, without the need to model the distribution of nucleation sites as well. On the other hand, it is poorly suited for the simulations interested in the study of the metastable stage of the phenomenon. [18]

#### 1.5.1.2 Step function

This model uses an empirical correlation for the flashing inception pressure  $P_{FI}$  to determine the lower nucleation limit. It assumes that all the nucleation sites are activated in the moment when the superheated condition is reached, and the concentration of bubble passes rapidly from a negligible to the maximum value. Using the classical homogeneous nucleation theory, some authors [19] derived a semi empirical correlation to calculate the pressure undershoot:

$$\Delta P_{FI} = P_{sat} - P_{FI} = \left[ \frac{16\pi\sigma^3}{3k_B T_c (1-v_l/v_g)^2 (Gb/\varphi)} \right]^{1/2} \quad (1.12)$$

where  $k_B$  is the Boltzmann constant,  $T_c$  is the critical temperature,  $v_l$  and  $v_g$  are the liquid and vapor specific volumes,  $Gb$  is the Gibbs number, and  $\varphi$  the heterogeneity factor. The ratio  $Gb/\varphi$  represents the flashing inception position, also obtained by empirical means. This method however does not define the extent of the zone where the nucleation takes place, that strongly depends on the initial condition of the flow, thus it is not capable to discriminate between different cases.

#### 1.5.1.3 Nucleation model

This model attempts to include the non-equilibrium zone with the introduction of a nucleation mechanism. As seen in previous sections, the flashing can be characterized by a heterogeneous or a homogeneous nucleation, but the nucleation process can take place on the surfaces of the container as well. The *homogeneous nucleation mechanism* is well described by the homogeneous nucleation theory, that can also be adapted to describe the *heterogeneous nucleation mechanism*; the nucleation rate per unit volume can then be defined as:

$$J_{het,B} = J_0 \cdot \exp(-Gb) \quad (1.13)$$

$$Gb = d_{cr} \cdot \varphi / k_B T_0 \quad (1.14)$$

$$J_0 = N_s B' \quad (1.15)$$

The Gibbs number is universal, and depends on the work necessary to create a bubble of critical size ( $d_{cr}$ ). The pre-exponential term ( $J_0$ ) is the number density of nucleation sites, and the relation (1.15) presents its general form. [18] The effective number density of heterogeneous sites  $N_s$  can be assumed equal to the number density of liquid molecules, or can be associated with the impurities dissolved inside of it.  $B'$  is rate of molecular interactions. The heterogeneous nucleation mechanism can also be expressed by statistical means using the *Probability Density Function* (PDF) of seeding nuclei inside the liquid, assuming they possess a normal size distribution:

$$\eta_b(r, r_{max}, \vartheta) = \frac{N_s}{\sqrt{2\pi\vartheta^2}} \exp\left(-\frac{(r-r_{max})^2}{2\vartheta^2}\right) \quad (1.16)$$

$$r_{max} = 2\sigma / (P_{sat} - P_{FI}) \quad (1.17)$$

$\vartheta$  is the standard deviation, and  $r$  is the nucleation site radius. The critical radius  $r_{max}$  is obtained through the flashing inception pressure. [20]

Wall nucleation is another important source of bubbles, and is acknowledged to be predominant even under adiabatic wall conditions. It is a complicate mechanism that depend on the wall features, as well as on the flow properties. The model differentiates between smoot and rough surfaces; for smooth walls the model can be derived from the heterogeneous nucleation relation (1.13), with a suitable modification that takes into account the contact angle between the wall and the liquid ( $\theta$ ) through the geometrical factor  $S = 0.5(1 + \cos \theta)$ :

$$J_{het,W} = N_s^{2/3} \cdot S \cdot B' \cdot \exp(-Gb) \quad (1.18)$$

For non-smooth walls the general approach is to make an analogy with the heated walls, where the bubble growth is driven by the superheated condition of the surrounding liquid, instead of the heat absorbed from the wall. Various author proposed different models. [21] [22] [23]

### 1.5.2 Bubble growth models

The growth of a spherical bubble inside of an infinite body of superheated liquid is governed by the Rayleigh-Plesset equation [10]:

$$\frac{P_b(T_b) - P_\infty(t)}{\rho_l} = R_b \frac{d^2 R_b}{dt^2} + \frac{3}{2} \left( \frac{dR_b}{dt} \right)^2 + \frac{4\nu_l}{R_b} \frac{dR_b}{dt} + \frac{2\sigma}{\rho_l R_b} \quad (1.19)$$

where the left-hand part of the equation presents the difference between the pressure of the vapor inside the bubble ( $P_b$ ), and the pressure of the liquid in

a point infinitely far from it ( $P_\infty$ ). The dynamics of bubble growth is the essential mechanism through which cavitation occurs. It differentiates two approaches: the *inertial controlled* and the *thermal controlled*.

#### 1.5.2.1 Inertial controlled

The inertial controlled approach neglects the cooling effect that the evaporation has on the liquid, and the vapour is assumed to be saturated. Under those conditions it becomes  $T_b = T_\infty = \text{const}$ , and  $P_b(T_b) = P_{sat}(T_\infty) = \text{const}$ . Furthermore, disregarding the surface tension ( $\sigma$ ) and the viscosity ( $\nu$ ) in the relation (1.19), the bubble growth rate can be expressed as:

$$\frac{dR_b}{dt} = \sqrt{\frac{2}{3} \frac{P_{sat}(T_\infty) - P_\infty(t)}{\rho_l}} \quad (1.20)$$

#### 1.5.2.2 Thermal controlled

In general, if the process is not extremely fast, the temperature of the liquid decreases during evaporation, and the temperature differential  $T_b - T_\infty$  is not constant, thus the bubble growth is determined by the energy balance at the vapor-liquid interface. This problem is nonlinear, so its solution can be found only numerically. For a simplified case though, an analytical solution has been proposed by some authors. [24] [25]

$$\frac{dR_b}{dt} = \sqrt{\frac{3}{\pi}} \cdot \frac{\rho_l C_P (T_\infty - T_{sat})}{\rho_g L} \cdot \sqrt{\frac{a_l}{t}} \quad (1.21)$$

this relationship can only be applied under assumptions that: there is no convection inside the liquid, that is inviscid and Newtonian; the pressure field is constant; the liquid is isothermal, and the temperature field is uniform; the only heat transfer takes place in the “thin thermal boundary layer” on the bubble surface, and it is purely conductive.

It also has been proposed that the relation between the inertial and the thermal term changes with time, with the inertial term that controls the bubble growth at the beginning of the reaction, while the thermal term takes over after a critical time:

$$t_{cr} = \frac{P_{sat}(T_\infty) - P_\infty(t)}{\rho_l} \cdot \frac{1}{\xi^2} \quad (1.22)$$

The parameter  $\xi$  is a thermo-physical quantity, and increases with the liquid temperature, making so that the thermal effect is predominant as the temperature raises. [26]

The bubble growth models however are difficult to implement inside the commercial CFD software, since those programs assume a shared pressure

field for all the fluids, so it is impossible to evaluate the pressure differential on the liquid-vapor interface, unless an additional momentum source is added. [10]

### 1.5.3 Vapor generation models

The modeling of vapor generation rate is a problem of particular interest for the numerical study of the flashing phenomenon. In literature, three methods have been presented.

#### 1.5.3.1 Homogeneous Relaxation Model (HRM)

The model has been successfully adopted by many authors [10], and it defines a relation for the volumetric vapor generation rate, treating the transition from the non-equilibrium to the equilibrium state as a relaxation process:

$$\Gamma_g = \left. \frac{\partial \rho}{\partial \chi} \right|_{P,h} \cdot \frac{d\chi}{dt} = \left. \frac{\partial \rho}{\partial \chi} \right|_{P,h} \cdot \left( \frac{\bar{\chi} - \chi}{\Theta} \right) \quad (1.23)$$

This relation takes into account the non-equilibrium effects of the system through the partial differential of  $\rho$ , that is the density of the vapor-liquid mixture.  $\chi$  is the vapor mass fraction, also defined as vapor quality, while  $\bar{\chi}(P, h)$  is its equilibrium value. The vapor quality ( $\chi$ ) and the void fraction ( $\alpha$ ) can be calculated from the density solution of the continuity equation:

$$\chi = \frac{\alpha \rho_g}{\rho}; \quad \alpha = \frac{\rho_l - \rho}{\rho_l - \rho_g} \quad (1.24)$$

The main aspect of the HRM is the correct definition of the relaxation time  $\Theta$ ; its empirical relation is [27]:

$$\Theta = \Theta_0 \alpha^a \psi^b \quad (1.25)$$

$$\psi = \frac{P_{sat} - P}{P_{crit} - P_{sat}}$$

Different values for the exponents have been proposed, based on the pressure of the system.

#### 1.5.3.2 Bubble growth model

This model uses the already mentioned bubble growth models (see Section 1.5.2) to estimate a vapor generation rate:

$$\Gamma_g = \rho_g N_b \cdot \frac{dV_b}{dt} = \rho_g A_i \cdot \frac{dR_b}{dt} \quad (1.26)$$

### 1.5.3.3 Interfacial exchange model

This general approach proposes that the phase change is governed exclusively by interphase heat transfer during evaporation, so the vapor generation rate only depends on the heat flux:

$$\Gamma_g = A_i \frac{\dot{q}}{L} \quad (1.27)$$

Where  $\dot{q}$  is the overall heat flux through the phase interface, and  $A_i$  is the interfacial area density. Assuming the temperature uniform inside the bubble, the heat flux can be defined as:

$$\dot{q} = h'_{tc}(T_l - T_{sat}) \quad (1.28)$$

Various empirical values have been proposed for the heat transfer coefficient  $h'_{tc}$ , but all limited to simplified cases. [10] Even the definition of the interfacial area density  $A_i$  presents several difficulties, as the bubble morphology (size, shape, distribution) varies as a function of flow characteristics.

## 1.6 Flashing flows modeling approach

The scope of this section is to present an overview of the various approaches employed in literature to model a flashing flow using either a system code, or a Computational Fluid Dynamic one; the latter are of particular interest because provide information about the spatial distribution of the phases. Depending on the level of complexity sought, several simplifications can be applied to the model: one major factor is to consider or not the thermal non-equilibrium effects between the phases, another one is to account for their relative velocity (mechanical equilibrium), important for the reliable calculation of interphase mass and heat transfer. [10]

### 1.6.1 Thermal equilibrium

This approach implies that the interphase heat transfer rate is infinite at the interface, so that the two phase are always in thermal equilibrium. ( $T_l = T_g$ ) Allowing for the relative velocities or not, the approach may follow two roads:

#### 1.6.1.1 Mechanical equilibrium

If the model assumes no relative velocity between the phases ( $\vec{U}_l = \vec{U}_g$ ), the fluid is treated as a pseudo single-phase mixture. This model is called HEM

(Homogeneous Equilibrium Model), and due to its simplicity has been widely used in the early versions of system codes such as RELAP. The condition of thermal equilibrium and no relative velocities can be applied in cases where the reaction time is very short, so that the phases cannot reach actual equilibrium. The model uses a 3-equation system, and the thermodynamic variables are obtained from interpolation tables. [10]

#### 1.6.1.2 Mechanical non-equilibrium

If void fraction exceeds the value of 0.3, ignoring the relative velocities between gas and liquid phase introduces significant errors. [28] The solution is to introduce an empirical correlation for the slip ratio:

$$S = a \left( \frac{\rho_l}{\rho_g} \right)^b \quad (1.29)$$

The pre-factor  $a$  is calculated empirically, and its value lies between 0.5 and 1, while the exponent  $b$  equals 1/2 for isentropic flows, and 1/3 for non-isentropic flows. [29] [30]

### 1.6.2 Thermal non-equilibrium

Empirical observations revealed that the discharge rate out of short length pipes are much larger than the one predicted by the HEM, and this discrepancy has been associated with the lack of thermal non-equilibrium ( $T_l \neq T_g$ ) effects. [31]

#### 1.6.2.1 Mechanical equilibrium

This approach aims to simulate the thermal non equilibrium effects, without accounting for the velocity differences of the phases. Some theoretical models have been development with this in mind.

##### 1.6.2.1.1 Boiling delayed model

This model uses the approach described in Section 1.5.1.2, where it assumes that all the nucleation sites are activated in the moment when the superheated condition is reached. The vapour generation rate is limited, as the flashing inception is delayed.

##### 1.6.2.1.2 HRM

The model has already been described in Section 1.5.3.1, and it tries to correct the HEM defining a relaxation process from non-equilibrium to equilibrium, over an empirical thermal relaxation time  $\Theta$ .

#### 1.6.2.1.3 Mixture model

This model has been developed by Blinkov et al. [32], and uses a 5- equations system: two continuity equations, for the mixture and the vapour, one momentum balance equation for the mixture, one energy equation for the liquid (the vapor is considered always in saturation condition), and one bubble transport equation. The closure is given by models for the vapor generation, the friction force, and the nucleation rate.

#### 1.6.2.2 Mechanical non-equilibrium

This condition is the more complete but also the more complex, as it takes into account both the thermal and mechanical non equilibrium effects. The mechanical non equilibrium is obtained by solving two different momentum balance equations, for both the liquid and gaseous phase. Disregarding the velocity difference between phases can lead to underestimation of the vapor generation rate.

##### 1.6.2.2.1 Drift flux model

The drift flux model, actually, does not solve the two momentum equations separately, but it approximates the velocity difference using other variables, such as void fraction and density, so it needs closure from semi-empirical relations for the drift velocity distribution. It is a good compromise between complexity and computational cost, as it can be implemented inside the frame of the HEM model, and it has been successfully used in simulation for nuclear applications. [33] Some authors have proposed a 5-equation drift flux model, where they solved two separated continuity equation for liquid and vapor (or for the mixture and the vapor), one momentum balance equation for the mixture, and two energy equation for the mixture and liquid (or for the liquid and the vapor). [34] [35] [36]

##### 1.6.2.2.2 Two-fluid model

To date is the more complete model: it uses a 6-equation system, solving the mass, the momentum, and the energy equations separately for both the liquid and the vapor phase. The relation between the phases (heat and mass transfer, relative mechanical interaction) are modelled through additional closure relations, that define the accuracy of the approach. Applying some assumptions (e.g., vapour always in saturated condition), the model can be reduced to a 5 or 4-equation system. The limits of the model must be sought in the closure relations. [10]

# 2 Modeling basis

## 2.1 Governing equations

The governing equations of fluid dynamics are the *Navier-Stokes Equations*, a non-linear system of partial differential equation, for which a general analytical solution in closed form, to date, does not exist. They can be expressed in a Eulerian (conservative) or Lagrangian (non-conservative) approach, and in differential or integral form. The integral form is considered to be “more fundamental” because it admits the presence of discontinuities inside the control volume, thus allowing the solution flow fields that contains shock waves. There are five governing equations of fluid dynamics: one for the *conservation of mass*, three for the *momentum balance*, and one for the *energy balance*. Given the number of variables, for the closure of the system is necessary to add some more relations, defined as *constitutive equations*: one is typically the *equation of state* for the fluid, another is the relation between the stress tensor and the velocity field, or the relation that links the thermodynamics variables.

### 2.1.1 Continuity equation

This equation is based on the principle that mass can neither be created nor destroyed, so it is derived by equating the net mass flux coming out of the surface of a control volume, with the reduction over time of the mass within it.

#### 2.1.1.1 Differential conservative form

$$\frac{\partial \rho}{\partial t} = \nabla \cdot (\rho \mathbf{V}) \quad (2.1)$$

#### 2.1.1.2 Integral conservative form

$$\frac{\partial}{\partial t} \int_V \rho dV + \int_S \rho \mathbf{V} \cdot \mathbf{n} dS = 0 \quad (2.2)$$

$\rho$  is the density,  $\mathbf{V}$  is the velocity vector,  $\mathbf{n}$  is the unit vector normal to the surface  $S$ , and  $V$  is the control volume. The two equations are equivalent, and one can transform the surface integral of the flux in (2.2) in the volume integral of the divergence in (2.1) simply applying the Gauss’s Theorem. The differential  $\partial/\partial t$  defines the time dependence for unsteady flows.

### 2.1.2 Momentum balance equations

Momentum balance is the extension of the Newton second law ( $F = ma$ ) to the case where the mass inside the control volume is not constant, and it states that the rate of change of the momentum of a body equals the net forces exerted on it:

$$d(m\mathbf{V}) = \mathbf{F}$$

To translate this statement into fluid mechanic terms, this law is applied to a control volume of fluid, where the forces exerted are the sum of the *volumetric forces*, that act directly on the mass contained in the volume (gravity, electro-magnetic forces), and the *surface forces*, that are applied on the surface of the volume (pressure, shear and normal stresses).

#### 2.1.2.1 Differential conservative form

$$\frac{\partial}{\partial t}(\rho u) + \nabla \cdot (\rho u \mathbf{V}) + \frac{\partial p}{\partial x} = \nabla \cdot \boldsymbol{\tau}_x + \rho f_x \quad (2.3)$$

$$\frac{\partial}{\partial t}(\rho v) + \nabla \cdot (\rho v \mathbf{V}) + \frac{\partial p}{\partial y} = \nabla \cdot \boldsymbol{\tau}_y + \rho f_y \quad (2.4)$$

$$\frac{\partial}{\partial t}(\rho w) + \nabla \cdot (\rho w \mathbf{V}) + \frac{\partial p}{\partial z} = \nabla \cdot \boldsymbol{\tau}_z + \rho f_z \quad (2.5)$$

That in compact form as a single vector equation becomes:

$$\frac{\partial}{\partial t}(\rho \mathbf{V}) + \nabla \cdot (\rho \mathbf{V} \mathbf{V}) + \nabla p = \nabla \cdot \bar{\boldsymbol{\tau}} + \rho \mathbf{f} \quad (2.6)$$

#### 2.1.2.2 Integral conservative form

$$\frac{\partial}{\partial t} \int_V \rho u dV + \int_S \rho u \mathbf{V} \cdot \mathbf{n} dS + \int_S p n_x dS = \int_S \boldsymbol{\tau}_x \cdot \mathbf{n} dS + \int_V \rho f_x dV \quad (2.7)$$

$$\frac{\partial}{\partial t} \int_V \rho v dV + \int_S \rho v \mathbf{V} \cdot \mathbf{n} dS + \int_S p n_y dS = \int_S \boldsymbol{\tau}_y \cdot \mathbf{n} dS + \int_V \rho f_y dV \quad (2.8)$$

$$\frac{\partial}{\partial t} \int_V \rho w dV + \int_S \rho w \mathbf{V} \cdot \mathbf{n} dS + \int_S p n_z dS = \int_S \boldsymbol{\tau}_z \cdot \mathbf{n} dS + \int_V \rho f_z dV \quad (2.9)$$

And in compact form:

$$\frac{\partial}{\partial t} \int_V \rho \mathbf{V} dV + \int_S \rho \mathbf{V} \mathbf{V} \cdot \mathbf{n} dS + \int_S p \bar{\mathbf{I}} \cdot \mathbf{n} dS = \int_S \bar{\boldsymbol{\tau}} \cdot \mathbf{n} dS + \int_V \rho \mathbf{f} dV \quad (2.10)$$

$u$ ,  $v$  and  $w$  are the components of the vector  $\mathbf{V}$  along the cartesian axis,  $p$  is the pressure,  $\bar{\boldsymbol{\tau}}$  is the viscous stress tensor,  $\mathbf{f}$  is the vector of volume forces per unit mass,  $\bar{\mathbf{I}}$  is the identity matrix. The notation with a double vector ( $\mathbf{V} \mathbf{V}$ ) has no mathematical meaning, but indicates that in the decomposition into directional components, the first vector must be changed in one of its components, while the second vector must be retained as such.

### 2.1.2.3 Shear stress for Newtonian fluids

A fluid is defined *Newtonian* if its shear stress is proportional to the deformation rate, that is, the velocity gradients. The relation for the shear stress is then defined as follows<sup>1</sup>:

$$\tau_{ij} = \lambda \frac{\partial u_k}{\partial x_k} \delta_{ij} + \mu \left( \frac{\partial u_i}{\partial x_j} + \frac{\partial u_j}{\partial x_i} \right) \quad (2.11)$$

The factor  $\delta_{ij}$  is the Kronecker delta

$$\delta_{ij} = \begin{cases} 0 & \text{if } i \neq j \\ 1 & \text{if } i = j \end{cases}$$

$\mu$  is the *dynamic viscosity*, and  $\lambda$  is called the *bulk viscosity*. In aerodynamic applications the *Stoke's hypothesis* can be enforced:

$$\lambda = -\frac{2}{3}\mu \quad (2.12)$$

The complete viscous stress tensor can be written as:

$$\begin{aligned} \bar{\boldsymbol{\tau}} &= \tau_x \hat{\mathbf{i}} + \tau_y \hat{\mathbf{j}} + \tau_z \hat{\mathbf{k}} \\ \tau_x &= \tau_{xx} \hat{\mathbf{i}} + \tau_{yx} \hat{\mathbf{j}} + \tau_{zx} \hat{\mathbf{k}} \\ \tau_y &= \tau_{xy} \hat{\mathbf{i}} + \tau_{yy} \hat{\mathbf{j}} + \tau_{zy} \hat{\mathbf{k}} \\ \tau_z &= \tau_{xz} \hat{\mathbf{i}} + \tau_{yz} \hat{\mathbf{j}} + \tau_{zz} \hat{\mathbf{k}} \end{aligned} \quad \rightarrow \quad \begin{aligned} \tau_{xx} &= \lambda \nabla \cdot \mathbf{V} + 2\mu \frac{\partial u}{\partial x} \\ \tau_{yy} &= \lambda \nabla \cdot \mathbf{V} + 2\mu \frac{\partial v}{\partial y} \\ \tau_{zz} &= \lambda \nabla \cdot \mathbf{V} + 2\mu \frac{\partial w}{\partial z} \\ \tau_{xy} &= \tau_{yx} = \mu \left( \frac{\partial u}{\partial y} + \frac{\partial v}{\partial x} \right) \\ \tau_{yz} &= \tau_{zy} = \mu \left( \frac{\partial v}{\partial z} + \frac{\partial w}{\partial y} \right) \\ \tau_{zx} &= \tau_{xz} = \mu \left( \frac{\partial w}{\partial x} + \frac{\partial u}{\partial z} \right) \end{aligned}$$

<sup>1</sup> The notation used is the Einstein convention, that presupposes the summation over repeated indexes, which assume the values 1,2,3 and refers to the vectorial components of the quantity:

$$\frac{\partial u_k}{\partial x_k} = \frac{\partial u}{\partial x} + \frac{\partial v}{\partial y} + \frac{\partial w}{\partial z} = \nabla \cdot \mathbf{V}$$

### 2.1.3 Energy Balance equation

Is based on the physical principle that energy is conserved, and is derived from the *First Principle of thermodynamics*:

$$de = \delta q + \delta L \quad (2.13)$$

$de$  is the rate of change of the total energy in the control volume,  $\delta q$  is the net heat flux toward the control volume, and  $\delta L$  is the work done on the control volume per unit of time by external forces. The total energy per unit volume is defined as:

$$E = \rho \left( e + \frac{1}{2} |\mathbf{V}|^2 \right) \quad (2.14)$$

where  $e$  is the internal energy per unit mass, and  $1/2 |\mathbf{V}|^2$  is the kinetic energy per unit mass, accounted when considering a moving fluid. The internal energy can be further expressed as function of the specific enthalpy  $h$ :

$$e = h - \frac{p}{\rho} \quad (2.15)$$

The energy balance equations can be then derived:

#### 2.1.3.1 Differential conservative form

$$\frac{\partial E}{\partial t} + \nabla \cdot [(E + p)\mathbf{V}] - \nabla \cdot (\bar{\boldsymbol{\tau}} \cdot \mathbf{V}) + \nabla \cdot \dot{\mathbf{q}} = \rho \dot{\xi} + \rho \mathbf{f} \cdot \mathbf{V} \quad (2.16)$$

#### 2.1.3.2 Integral conservative form

$$\begin{aligned} \int_V \frac{\partial E}{\partial t} dV + \int_S (E + p)\mathbf{V} \cdot \mathbf{n} dS - \int_S (\bar{\boldsymbol{\tau}} \cdot \mathbf{V}) \cdot \mathbf{n} dS + \int_S \dot{\mathbf{q}} \cdot \mathbf{n} dS \\ = \int_V \rho \dot{\xi} dV + \int_V \rho \mathbf{f} \cdot \mathbf{V} dV \end{aligned} \quad (2.17)$$

$\dot{\mathbf{q}}$  is the heat flux due to thermal conduction, and depends on the temperature gradient through the *Fourier's law*:

$$\dot{\mathbf{q}} = -k\nabla T \quad (2.18)$$

$\dot{\xi}$  is the heat absorbed per unit of time and unit of mass,  $\bar{\boldsymbol{\tau}} \cdot \mathbf{V}$  is the work done by the surface forces, and  $\mathbf{f} \cdot \mathbf{V}$  is the work done by the volumetric forces on the control volume.

### 2.1.4 Equations of state

The equations of state relate the density and the internal energy to the basic thermodynamic variables pressure and temperature. Several alternatives are available, depending on the assumptions made.

#### 2.1.4.1 Ideal gas

In typical aerodynamic applications it can be assumed that the gas behaves like a perfect gas, so it responds to the perfect gas law:

$$p = \rho \frac{\mathcal{R}}{M} T = \rho R T \quad (2.19)$$

$\mathcal{R} = 8.314 J/mol K$  is the universal gas constant,  $M$  is the molecular weight,  $R = \mathcal{R}/M$  is the specific gas constant, and  $T$  is the temperature. The perfect gas law treats the gas molecules as point particles that do not occupy volume, and interacts with the container, but not with each other.

#### 2.1.4.2 Real gas

At high pressure and low temperature, the intermolecular attractive force between gas particle becomes less negligible, and the gas behaviour deviates from that predicted by the perfect gas law. Van der Waals modified this law to account for the volume that the gas particles occupy, deriving the already cited equation:

$$\left( P + \frac{an^2}{V^2} \right) (V - nb) = nRT \quad (1.5)$$

The first factor on the right-hand side is modified to account for the molecular interaction, while the second factor accounts for the volume occupied by the molecules.  $n$  is the number of gas moles, while the gas characteristic constants  $a$  and  $b$  are obtained through experimental observations.

#### 2.1.4.3 IAPWS-IF97

The “*International Association for the Properties of Water and Steam, Industrial Formulation 1997*” is a formulation for the thermodynamic properties of water and steam for industrial use, that is widely used to run CFD codes. The formulation divides the p-T diagram of water into several region, each of which is defined by a different fundamental polynomial equation. The combination of these equations and their derivatives allows the calculation of any thermodynamic property of the fluid (specific volume, internal energy, entropy, enthalpy, speed of sound, etc.). [37] The limits of the formulation are represented in Figure 2-1 [38].

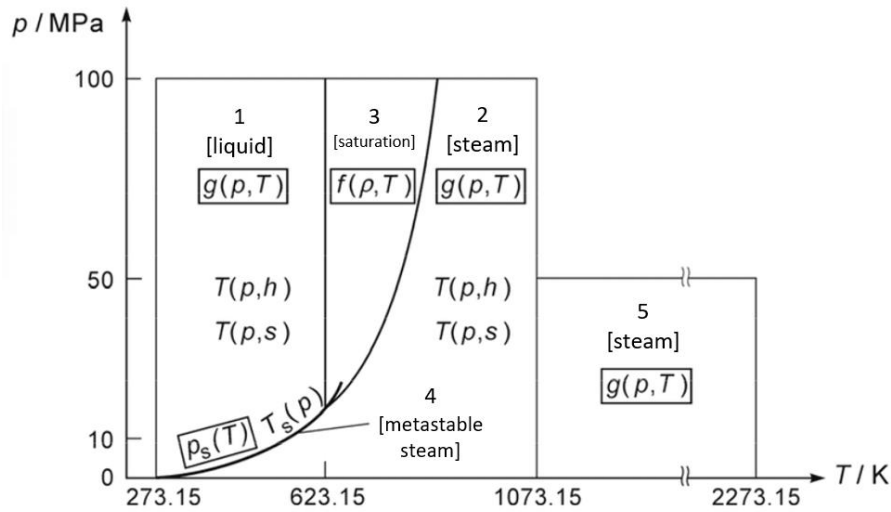


Figure 2-1 – Regions of the IAPWS-IF97 formulation

### 2.1.5 Turbulence

At high Reynolds number ( $Re \cong 3500$ ) the flow enters the turbulent regime, and as already mentioned in Section 1.4.4.1, this effects the jet characteristics, as the turbulence increases the entrainment of the external air, and enhances the mixing of the droplets inside the jet. An accurate modeling of the turbulent effects is important in the prediction of the development of the flashing jet. Three main approaches exist to numerically simulate a turbulent flow: DNS, LES and RANS.

The Direct Numerical Simulation (DNS) approach is the most accurate one, as it numerically solves the Navier-Stokes equations, obtaining a time-dependent velocity field. In order to resolve both the timescale and the length-scale of the turbulence, the spatial and temporal resolutions of the simulation need to be very fine:

$$\Delta x_{DNS} \propto Re^{-3/4} \quad \Delta t_{DNS} \propto Re^{-1/2}$$

The computational cost increases steeply with the Reynolds number ( $\propto Re^3$ ), so this approach is limited for the solution of flow with small domains and low to moderate Reynolds numbers.

In Large-Eddy Simulations (LES) the smaller-scale fluctuations are separated from the large unsteady turbulent motion through a spatial filter. The dynamics of the large-scale motions are computed explicitly, while the effects of the small-scale are described through a sub-grid model. LES is computationally more efficient than DNS, as it spends the computing capacity to solve the large anisotropic turbulent motions, instead of the small, dissipative ones. [39]

### 2.1.5.1 RANS method

RANS uses a similar approach to LES, but instead of using a filter, it applies the Reynolds decomposition, where the velocity and the pressure fields are decomposed into their mean values, and a fluctuating component.

$$u_i = \langle U_i \rangle + u'_i \quad p = \langle P \rangle + p'$$

Substituting the decomposed quantities into the Navier-Stokes equations, and then averaging, the result is a new set of equation, called *Raynolds Averaged Navier-Stokes* (RANS). In the case of an incompressible flow:

$$\frac{\partial \langle U_i \rangle}{\partial x_i} = 0 \quad \frac{\partial u'_i}{\partial x_i} = 0 \quad (2.20)$$

$$\frac{\partial \langle U_i \rangle}{\partial t} + \langle U_j \rangle \frac{\partial \langle U_i \rangle}{\partial x_j} = -\frac{1}{\rho} \frac{\partial \langle P \rangle}{\partial x_i} + \nu \frac{\partial^2 \langle U_i \rangle}{\partial x_j \partial x_j} - \frac{\partial \langle u'_i u'_j \rangle}{\partial x_j} \quad (2.21)$$

The equations (2.20) shows that the continuity equation is satisfied by both the mean field, and the fluctuation velocities. The momentum equation (2.21) presents a new additional term, that correlates the components of the fluctuating velocities: the *Reynolds stress tensor*  $\langle u'_i u'_j \rangle$ . This term represents the influence that the turbulent fluctuating velocities have on the mean field, by means of a virtual stress that exerts a fictitious force. However, the presence of the unknown Reynolds stresses poses a closure problem on the 4-equation Reynolds system, so the extra term needs to be otherwise determined. There are two main approaches: one is to apply the *Turbulence viscosity hypothesis*, developed by Boussinesq in 1887, the other is to use the *Reynolds-stress transport equation*, that uses an ad hoc equation to model the transport of the Reynold stress tensor  $\langle u'_i u'_j \rangle$  inside the flow.

#### 2.1.5.1.1 Turbulent Viscosity Hypothesis (TVH)

The TVH proposes a relation between the stress tensor and the mean velocity gradients:

$$\langle u'_i u'_j \rangle - \frac{2}{3} k \delta_{ij} = -\nu_T \left( \frac{\partial \langle U_i \rangle}{\partial x_j} + \frac{\partial \langle U_j \rangle}{\partial x_i} \right) = -2\nu_T \bar{S}_{ij} \quad (2.22)$$

$k = \langle u'_i u'_i \rangle / 2$  is the mean turbulent kinetic energy,  $\bar{S}_{ij}$  is the mean rate-of-strain tensor, analogous to the one in the viscous stress in a Newtonian fluid (2.11), and  $\nu_T$  is the *turbulent viscosity*. In general, the TVH is reasonable only for simple shear flows, in which the turbulence characteristics evolve relatively slowly (e.g., round jet, mixing layer, channel flow, boundary layer). [39] Once adopted the TVH, in order to provide a closure for the Reynold equations, a *turbulence model* is needed to define an expression for the turbulent viscosity  $\nu_T$ . Several alternatives exist, including one-equation models (Spallart-Allmaras model, Baldwin-Barth model), or two-equations models ( $k - \varepsilon$ ,  $k - \omega$ ).

### 2.1.5.1.2 $k - \varepsilon$ model

The  $k - \varepsilon$  model is a two-equation model that defines the turbulent viscosity as a function of the turbulent kinetic energy  $k$  and the turbulent dissipation rate  $\varepsilon$ . A transport equation is solved for each of those quantities.

$$\nu_T = C_\mu \frac{k^2}{\varepsilon} \quad (2.23)$$

$$\frac{\partial k}{\partial t} + U_i \frac{\partial k}{\partial x_i} = \Pi - \varepsilon - \frac{\partial I_i}{\partial x_i} \quad (2.24)$$

$$\frac{\partial \varepsilon}{\partial t} + U_i \frac{\partial \varepsilon}{\partial x_i} = C_{\varepsilon 1} \frac{\varepsilon}{k} \Pi - C_{\varepsilon 2} \frac{\varepsilon^2}{k} + \frac{\partial}{\partial x_i} \left( \frac{\nu_T}{\sigma_\varepsilon} \frac{\partial \varepsilon}{\partial x_i} \right) \quad (2.25)$$

$$I_i = -\frac{\nu_T}{\sigma_k} \frac{\partial k}{\partial x_i}; \quad \Pi = -\langle u'_i u'_j \rangle \frac{\partial U_i}{\partial x_j} \quad (2.26)$$

$I_i$  is the diffusion term,  $\Pi$  is the production term, the other parameters can be adjusted to improve the accuracy depending on the setting. The standard values represent a compromise for good performances over a large range of flows, and are obtained by the empirical fitting of prediction and experiments:

$$C_\mu = 0.09; \quad C_{\varepsilon 1} = 1.44; \quad C_{\varepsilon 2} = 1.92; \quad \sigma_k = 1.0; \quad \sigma_\varepsilon = 1.3$$

$k - \varepsilon$  model is the most widely used turbulence model, it is incorporated in most commercial CFD codes, and it has been successfully adopted for several problems, including multiphase flows. However, the model accuracy is subjected to the turbulent viscosity hypothesis limitations. [39]

## 2.2 CFD

Computational Fluid Dynamics is the method of solving fluid flow problems using numerical analysis and algorithms. The overall approach is to approximate the general governing equations of the flow by a system of algebraic equations for the variables, and solve the system for a set of spatial and temporal discrete locations. The most popular spatial discretization method are the *finite differences* (FD) and the *finite volumes* (FV).

The FD method uses the differential form of the Navier-Stokes equations as a starting point, and the discretization idea comes from the definition of derivative. The geometric domain is discretized using a structured grid, and the variables are calculated on the grid nodes, while the derivatives are approximated using the Taylor series expansions. The FV method is based on the integral form of the N-S equations, so the physical domain is discretized in finite volumes, i.e., cells, where the computational node is assigned to the centre of each cell. The definition of the boundary conditions, that is the imposed restrictions on the border of the geometric domain, and the initial condition, completes the equation system.

The system can be composed by ordinary differential equations in case of unsteady problems (time-dependant), or by algebraic equations for steady flows. For unsteady problems, such as transient simulation, the total time of the event is subdivided into smaller intervals, called time-steps; the solution is then calculated at each time-step using the solution of previous ones. Different schemes exist to advance the solution in this manner: if the solution at the current time-step is calculated using only the solution at the previous time-step, the scheme is called *explicit*; if the solution at the current time step uses both the solution at previous time-steps, and the solution of the current time step, the scheme is called *implicit*. Furthermore, depending on the number of previous time-step solutions used, the temporal scheme can be of first-order (only one previous time-step solution, that is the Euler method), second-order (two previous time-steps), or fourth-order (four previous time-steps). As an example, simple first-order schemes are reported:

$$\text{Euler explicit} \quad y_{k+1} = y_k + h f(t_k, y_k) \quad (2.27)$$

$$\text{Euler implicit} \quad y_{k+1} = y_k + h f(t_k, y_k, y_{k+1}) \quad (2.28)$$

$y_{k+1}$  is the solution at the  $(k + 1)^{th}$  time-step, the one being calculated, while  $y_k$  is the solution at the  $k^{th}$ ;  $f$  is the equation to be solved, and it can be function of the previous solution  $y_k$  or the current one  $y_{k+1}$ ;  $t_k$  is the total time at the  $k^{th}$  time-step, and  $h$  is the temporal dimension of the time-step.

### 2.2.1 STAR-CCM+

The software employed for this work is STAR-CCM+ version 2021.1.1 (the acronym stands for: *Simulation of Turbulent flow in Arbitrary Regions - Computational Continuum Mechanics*). It is a Computational Aided Engineering (CAE) solution developed by CD-Adapco, capable of solving a range of engineering problems, both in fluid and in solid continuum mechanics, including multi-physics such as fluid through porous media, multiphase flows, non-Newtonian fluids, turbulence, viscoelasticity, etc. Furthermore, it provides a suite of integrated components that allows to carry out the whole engineering analysis, starting from the CAD creations and mesh generation, up to the post-processing and the results analysis. [40]

The physics is defined through a selection of solvers, that identify the physics continuum of the simulation. Selecting the right solver and the right models, STAR CCM+ is capable of modeling flows that are:

- 2D, axisymmetric, 3D
- Inviscid, laminar, or turbulent
- Newtonian or non-Newtonian
- Incompressible or compressible

- Single-phase or multi-phase
- Single-component or multi-component mixtures
- Gravitational accelerated
- Steady or Unsteady
- Constant density, ideal gas law, or real gas law

Furthermore, for every type of flow STAR-CCM+ provides several models that further allow the specialisation of the simulation. The discretization method employed is usually the finite volume approach, and the solution of the simulation can be carried out with different energy modeling approaches:

- The *Segregated Flow model* solves the integral momentum balance equations in sequence, and then links the results with the continuity equation constrains on the velocity field using a pressure-correction equation. STAR-CCM+ implements two pressure-velocity coupling algorithms: SIMPLE and PISO. The energy equation is then solved on his own, either with the enthalpy or the temperature formulation.
- The *Coupled Flow model* solves the continuity, momentum, and energy in a coupled manner, that is, they are solved as a vector of equation.

In the interest of this work is interesting to analyse the alternatives offered by the software for the simulation of multiphase flows.

## 2.2.2 *Multiphase flows models*

STAR-CCM+ offers a comprehensive suite of multiphase models, sufficient to cover all multiphase regimes in real world problems, that can be used in combination with other physics models, in order to accurately simulate complex physics. [41] The models can be split into two families: the Eulerian Models, that uses a conservative formulation, where the fluid is treated as a continuum that flows inside a fixed volume; and the Lagrangian Models, where it simulates the single particle moving through space and time in a non-conservative approach. [40]

### 2.2.2.1 *Eulerian Multiphase (EMP) Model*

The EMP considers each phase as an interpenetrating continuum, meaning that the phases are mixed on a length scale smaller than the resolution of the computational grid. All the phases exist in the same cell, so the effective volume occupied by a single phase is given by the volume fraction. The continuity, momentum, and energy equations are solved for each phase, while the pressure field is the same for all the phases. The closure for the conservation equations is given by the phase interaction models, that define the interphase energy, momentum, and mass transfer.

#### *2.2.2.2 Mixture multiphase (MMP) Model*

MMP is a computationally lighter version of the EMP, as it considers the phases miscible, so it can solve a single set of conservation equation for the whole mixture rather than for each phase separately. It cannot resolve the interface between the phases, but it can model the slip velocity. Is not suitable for simulation where there is a large variation between the phase's quantities.

#### *2.2.2.3 Volume of Fluid (VOF) Model*

VOF is a simple multiphase model that utilises a Eulerian framework to simulate the flow, where each phase constitutes a large structure, and is used to solve the interface between immiscible fluids. Is also indicated for the simulation of various liquid-vapor phase changes, such as boiling, evaporation/condensation, and cavitation. The model also implements the Homogeneous Relaxation Model (see in Section 1.5.3.1), advised for the simulation of the flash boiling phenomenon.

#### *2.2.2.4 Lagrangian Multiphase (LMP) Model*

LMP can be considered a hybrid approach, as it solves the Navier-Stokes equations for the continuum phase using a Eulerian formulation, and uses a Lagrangian approach to solve the equation of motion of the dispersed phase as it passes through the system in the form of particle-like elements. It is suited for simulations where the continuum carries a relatively small volume of discrete particles, droplets, or bubbles.

#### *2.2.2.5 Dispersed Multiphase (DMP) Model*

DMP combines some aspects of both the EMP and LMP, as it simulates a dispersed phase, but using a Eulerian formulation. The continuum phase is resolved with single-phase models. By default, the coupling between the phases is one-way, meaning that only the continuum phase influences the dispersed phase. When the optional two-way coupling is active, the dispersed phase can influence the continuum. This model is suited for simulating flows loaded with small droplets or bubbles.

#### *2.2.2.6 Fluid Film Model*

It belongs to the Eulerian models' family, and is used for the simulation of the behaviour of a thin layer of fluid on a solid surface. It can be used together with the LMP, EMP or DMP models, and is suited to simulate rivulets and other surface tension effects.

## Chapter 2

# 3 Model development and validation

### 3.1 Publication considered for this work

The CFD model developed in this work was based on the technical report of Akihiko Minato et al. “Numerical Study of Two-Dimensional Structure in Critical Steam-Water Two-Phase Flow”, published in 1995 in the *Journal of Nuclear Science and Technology*. [42] Scope of the work was to study the structure of a two-phase discharge flow as a part of a safety research of water-cooled nuclear reactors. The numerical simulation developed uses the *two-fluid model* (see Section 1.6.2.2.2) to investigate the difference between one and two-dimensional flow effects in the first few milliseconds after the break. The work used the quasi-steady flow conditions of the “Marviken full-scale Critical Two Flow” test n° 7 after 7 second from release. The Marviken CFT Tests are a series of full-scale water-discharge experiments conducted in 1978-1979 at the Marviken Power Station plant, a former nuclear reactor located in Sweden, repurposed as experimental facility. [43]

The Minato’s report [42] was selected because of its similarity with the configuration of interest for this work: it presents a computational domain of simple geometry, and uses as a working fluid sub-cooled water under similar initial thermodynamical conditions.

## 3.2 CFD modeling procedure

The CFD modeling procedure using STAR-CCM+ present several stages:

- Import or creation of the geometry
- Meshing of the computational domain
- Selection of the physics models
- Definition of the boundary and initial conditions
- Setting up solvers
- Running the simulation
- Post-processing (creation of scenes, plots, and reports)

### 3.2.1 Geometry

The geometry was defined using the STAR-CCM+ integrated 3D-CAD module, and was generated according to the configuration of the two-dimensional Case B of the Minato's work, as it was stated that the presence of the pressure vessel before the pipe returned a more realistic flow configuration both inside the pipe, and in the open space. In Figure 3-1 is presented the base geometry, together with the dimensions used for the vessel and the discharge pipe.

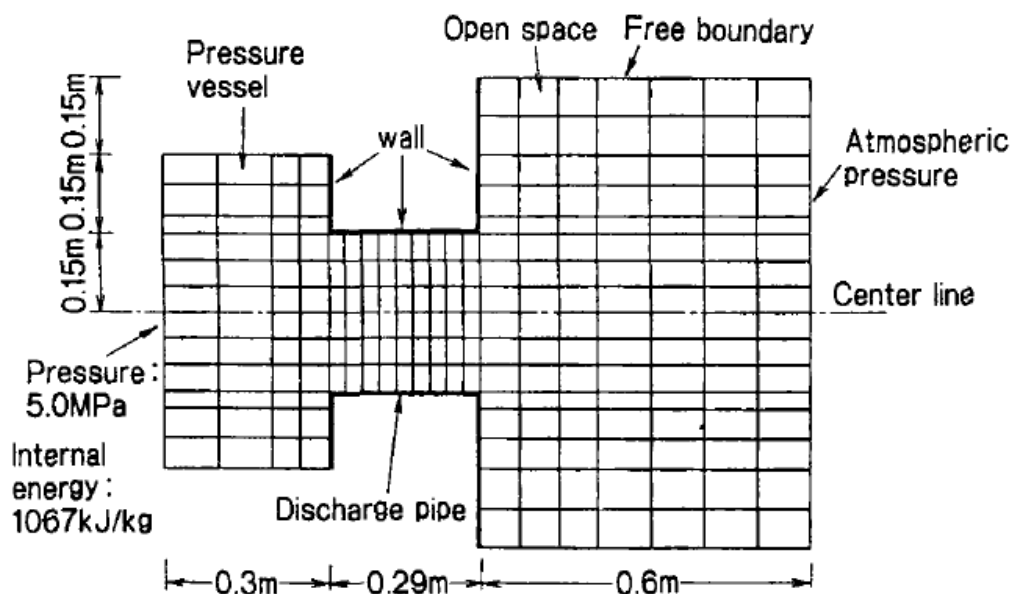


Figure 3-1 – Minato geometry - Case B

Being that the configuration presents an axial symmetry, the simulation was performed only on half of the Case B geometry, enforcing a symmetry condition on the central axis. The open space portion of the domain was modified into a quarter circle shape, with 15 m of radius, to allow a free expansion of the flow, without the risk of it being disturbed by any spurious, numerical or acoustic, reflected waves coming from the outlet. For a 2D simulation, the CAD is generated extruding a sketch by a negligible quantity, as the simulation is performed only on the  $z = 0$  surface.

Once the domain geometry is defined, it is imported inside the simulation environment through the definition of the *geometry parts*, which contain the geometry data needed for meshing. The domain geometry part is divided into *surface parts* and *curve parts*; each geometry surface is assigned to a different surface part. The parts are a geometrical entity, so in order to define a fluid field, the domain part is related to a Region, defined as a volume domain completely surrounded by boundaries. [40]

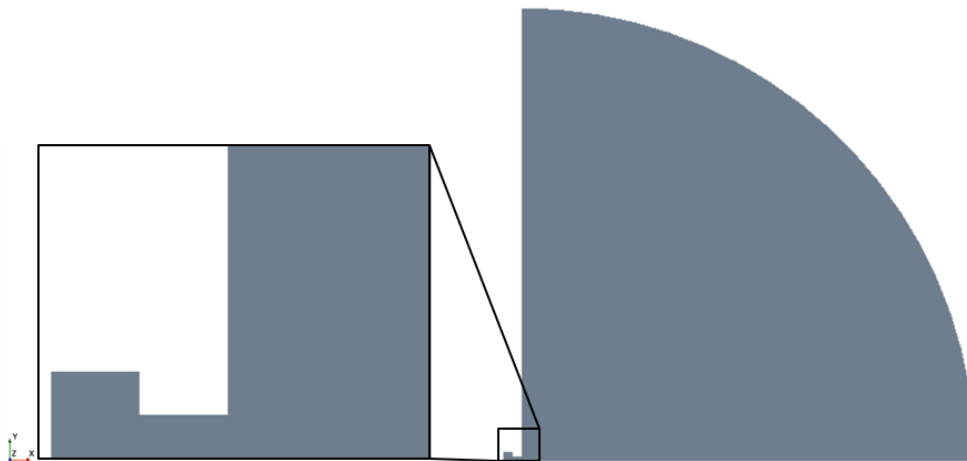


Figure 3-2 – Model geometry - Complete domain (right), pipe and vessel (left)

### 3.2.2 Mesh

A mesh is the discretization of the physical domain, that allow the solution of the governing equation using a finite volume formulation. To create a 2D mesh is necessary to mark the surface part that contain the  $z = 0$  plane, using the operation *Badge for 2D meshing*. It was then used the *Automated mesh (2D)* function to create the mesh solver. The Automated mesh (2D) Operation dialog expands into 3 nodes, that allow the definition of the mesh topology:

- Meshers: allows the selection of the Volume Mesher (Polygonal, Quadrilateral, or Triangular), with the optional Prism Layer Mesh. For the simulation was used the Polygonal Mesher. The mesher can be also set to adapt the cell dimensions according to a Table: this function is the basis for the Adaptive Mesh Refinement.
- Default Controls: this node allows the definition of the cell dimensions inside the mesh. It lets specify the minimum and target cell size, together with the growth rate and surface curvature and proximity.
- Custom controls: it allows the definition of a curve, surface, or volumetric control over the mesh

A mesh cell size needs to be small enough to be able to capture the flow characteristics for a given time-step. In Computational Fluid Dynamics the rule-of-thumb is given by the Courant Number (also known as the Courant-Friedrichs-Lax, CFL, number):

$$CFL = \frac{v\Delta t}{\Delta x} < 1 \quad (3.1)$$

$v$  is the local velocity,  $\Delta t$  is the time-step, and  $\Delta x$  is the local cell size. It defines the upper limit a CFD simulation should respect, as it relates the velocity of the real flow ( $v$ ) with the velocity of the calculation ( $\Delta x/\Delta t$ ); a flow faster than the calculation ( $CFL > 1$ ) means that a fluid particle can jump from a computational cell to another, without passing through the intermediate cells, generating a numerical error in the simulation, as apparently it is not obeying the conserving equations. A bigger cell size makes it easier to comply with the CFL limit, but returns a poor resolution of the flow; a small cell size gives a better result, but meshing very finely the entire computational domain (e.g., cell with  $1 \text{ mm}^2$  surface) would create more than 150 million cells, that would slow the simulation unnecessarily, as the vast majority of the cell would be solving a still, or very slow, fluid. The solution is to refine the mesh only where needed, and leave the rest of the domain coarse. Given the transient characteristic of the flow, this cannot be achieved using a static mesh, so a mesh adaptivity strategy need to be employed.

### 3.2.2.1 Static mesh optimization

The initial mesh needs to be finer near the inlet, and coarser toward the downstream borders. To achieve this, the inlet region of the domain, that is the vessel and the pipe, have been finely meshed using a static mesh approach. To do so, a cylinder and a sphere shape part has been created, and used as input parts for a *volumetric custom control*, setting the custom size value equal to the minimum target cell size (3.3). On the outlet boundary, a *custom target cell size control* has been enforced, and set to the maximum target cell size value (3.4).

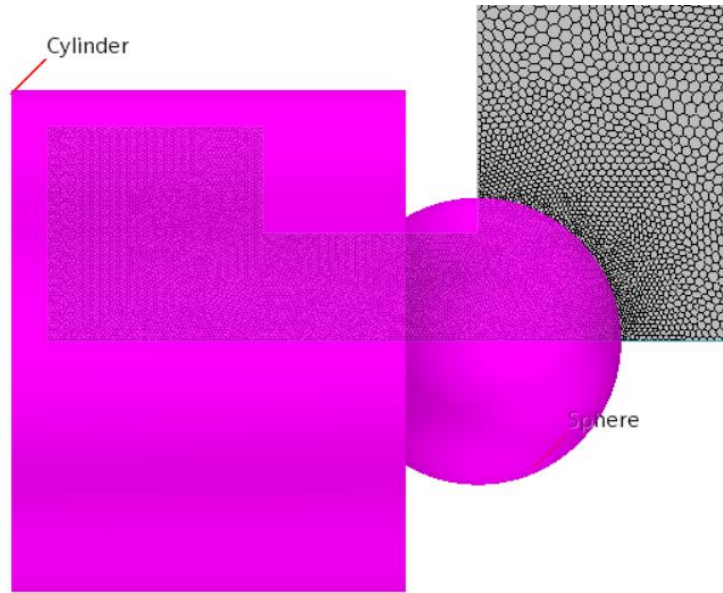


Figure 3-3 – Cylinder and Sphere volumetric custom controls

### 3.2.2.2 Adaptive mesh refinement

STAR-CCM+ implements an Adaptive Mesh Refinement (AMR) model that refines or coarsens the cells based on adaptive mesh criteria. However, this model is not compatible with the 2D meshes, so for this work the mesh adaptivity strategy has been adapted starting from the one used by Zappatore et al. in [44]. Using the user-defined field functions option, various quantities have been introduced. The representative dimension of a polygonal cell was defined starting from the volume of the cell  $V_c$  as:

$$\delta_c = \sqrt{V_c} \quad (3.2)$$

The minimum and maximum target cell size have been defined as:

$$\delta_{min} = 0.003 \text{ m} \quad (3.3)$$

$$\delta_{max} = \min(10 \delta_c, 0.1) \text{ m} \quad (3.4)$$

the maximum cell size definition allows for a smoother coarsening of the regions previously refined, as increases the cell size up to a value, selected as the minimum between 0.1, and 10 times the current cell dimension. The quantity selected to drive the mesh adaptation is the Mach number, and in particular its variation, which allows to increase the refinement of the mesh in the locations with both velocity and temperature steep variations:

$$\Delta M = |\nabla M| \delta_c \quad (3.5)$$

The refinement based on the Mach variation is obtained defining a refined cell size, that does not account for the minimum and maximum limitations, but only on the current cell dimension:

$$\delta_{c,ref} = \frac{10^{-2}}{\Delta M} \delta_c \quad (3.6)$$

Finally, the target cell size is defined, imposing a Mach variation threshold:

$$\delta_{c,target} = \begin{cases} \max(\delta_{c,ref}, \delta_{min}) & \text{if } \Delta M > 0.1 \\ \min(\max(\delta_{c,ref}, \delta_{min}), \delta_{max}) & \text{if } \Delta M \leq 0.1 \end{cases} \quad (3.7)$$

If in a given cell the Mach variation is above the threshold, the cell needs to be refined, so the target cell size assumes the maximum value between the refined cell size and the minimum target cell size, in order to limit the minimum possible dimension of the cell. If the Mach variation is below the threshold, the cell target size increases, up to the maximum possible value for that cell. Once defined, the target cell size values are used to compile a *XYZ Internal Table*, that is then used by the polygonal mesher as a Refinement Table. In order to continuously follow the propagation of the flow, this procedure needs to be repeated after a certain number of time-steps, so the algorithm was automatized by means of a macro. STAR-CCM+ allows the direct registration of the macro during the simulation; the macro recorded was then modified to repeat the following steps:

1. Run the simulation for 100 time-steps
2. Extract the values of  $\delta_{c,target}$  and compile the XYZ Internal Table
3. Execute the Polygonal Mesher
4. Repeat until Stopping Criteria is reached

The adapted mesh after 1 ms of simulation is presented in Figure 3-4

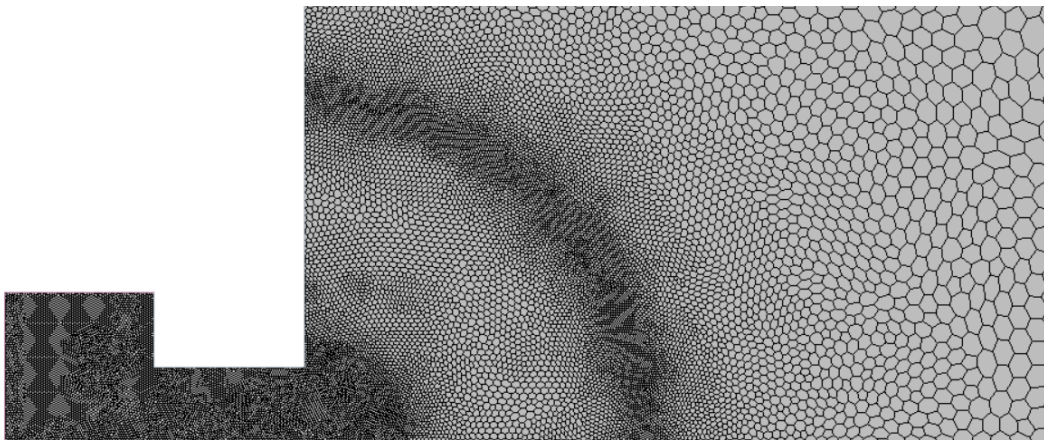


Figure 3-4 – Mesh adaptation after 1ms

### 3.2.3 *Physics models and solvers*

The physics models are selected during the creation of the physic continuum, that is the material present inside the domain region. This work aims to simulate the phase transition from water to vapor, that fill the whole domain, so the definition of a single physics continuum was enough. The model selected are listed below, some recommended models are automatically selected by the software:

- Two Dimensional
- Eulerian Multiphase
- Volume of Fluid (VOF)
- Multiphase Interaction
- Multiphase Equation of State
- Segregated Flow
- Segregated Multiphase Temperature
- Implicit Unsteady
- Turbulent
- Reynolds-Averaged Navier-Stokes
- K-Epsilon Turbulence
- Solution Interpolation
- Gradients

#### 3.2.3.1 *Eulerian phases*

STAR CCM+ simplified the definition of a multiphase material by grouping the Eulerian family of multiphase models (see Section 2.2.2) into four categories: EMP, MMP, VOF and Two-Phase Thermodynamic Equilibrium. The selection of any of those insert the simulation into a Eulerian framework, where each phase is treated as a continuum. If needed, the Lagrangian phases can then be dispersed inside the Eulerian continuum. For this simulation the choice was to use the VOF model (see Section 3.2.3.3), so the phases are resolved using a Eulerian approach. Each phase needs to be created inside a Eulerian Phases sub-node, where the characteristics of the phase can be selected, in order to outline its physical formulation. A phase requires at least the material model, the equation of state, and the viscous regime: for both water and vapor the IAPWS-IF97 formulation was used, and the turbulent model selected; water was then defined as liquid, vapor as gas.

### 3.2.3.2 Segregated Flow and Energy

The Segregated Flow model was selected automatically after the multiphase VOF model definition. It solves the governing equation in a sequential manner, using a pressure-velocity coupling algorithm to fulfil the mass conservation constrain. The algorithm used is the SIMPLE (Semi-Implicit Pressure Linked Equation), which allows a better flexibility on the selection of the time-step, resulting in more stable simulation. The overall formulation, even though is not the best solution for highly compressible flows, allows for the fine tuning of the solver parameters, such as the Under-Relaxation Factors. Together with the Segregated Flow, to solve the energy conservation equation the Segregated Fluid Energy model is needed; it proposes three formulations: Segregated Fluid Enthalpy (recommended for simulation involving combustions), Segregated Fluid Temperature, and Segregated Fluid Isothermal (recommended for simulation with small temperature variation). For the simulation the model selected was the Segregated Fluid Temperature, that solves the energy conservation equation with the total energy formulation, and then calculates the enthalpy using the equation of state. The volume discretization scheme for the convection in both the Segregated Flow and Segregated Energy models were left with the default 2<sup>nd</sup>-order upwind scheme. Regarding solver settings, the Algebraic Multi-Grid (AMG) Linear Solver Cycle Type was changed from the default type to the F-cycle, that uses more internal cycles among the different grid levels, losing in computational efficiency but earning in accuracy and robustness. For the same reason, all the default Acceleration Methods were disactivated. [44]

### 3.2.3.3 Volume of Fluid (VOF)

For the solution of the Multiphase flow, the VOF model (see Section 2.2.2.3) was selected, as it was advised in the STAR-CCM+ User Manual [40] as a suitable model for configurations where each phases constitute a large structure, and are separated by an interface: in the simulation of interest for this work, the water is only present inside the pipe and the vessel, while the rest of the domain is filled with vapor, and all the phase transition phenomena occurs at the interface, making the VOF model a good candidate. The VOF model furthermore allows the activation of a *compressibility enhancement* option, that improves the model ability to solve highly compressible flows ( $M > 0.3$ ) by switching from a centred to an upwind reconstruction approach when evaluating the gas density inside a cell. The volume discretization scheme for the convection used by the VOF model is the High-Resolution Interface Capturing (HRIC), that solves the convective transport of immiscible fluids that remains separated by a sharp interface. The Segregated VOF solver then solves a discretized conservation equation for the volume fraction of each phase. The volume fraction transport equation is:

$$\frac{\partial}{\partial t} \int_V \alpha_i dV + \int_A \alpha_i \mathbf{V} \cdot d\mathbf{a} = \int_V \left( S_{\alpha_i} - \frac{\alpha_i D\rho_i}{\rho_i} \frac{D}{Dt} \right) dV - \int_V \frac{1}{\rho_i} \nabla \cdot (\alpha_i \rho_i \mathbf{V}_{d,i}) dV \quad (3.8)$$

where  $\alpha_i = V_i/V$  is the  $i$ -th phase volume fraction ( $V_i$  is the volume of the phase,  $V$  is the volume of the cell),  $\mathbf{a}$  is the surface area vector,  $\mathbf{V}$  is the mixture mass-averaged velocity,  $\mathbf{V}_{d,i}$  is the diffusion velocity, and  $S_{\alpha_i}$  is a user-defined source term. When the VOF phases are only two, the model solves the equation for the first phase only, and then adjust the second phase volume fraction so that the total sum on each cell equals 1. [40]

### 3.2.3.4 Multiphase interaction

The multiphase model also allows the selection of a Multiphase Interaction, so the Homogeneous Relaxation Model (HRM – see Section 1.6.2.1.2) was selected, as it was advised for the modeling of the thermal non-equilibrium vaporization mechanisms [40], ranging from the cavitation inside a pipe, to the flash boiling of superheated water into steam, like inside a Pressurised Water Reactor (PWR). The model solves a finite rate equation for the rate of change of the vapor mass fraction [40]:

$$\frac{d\chi}{dt} = \frac{\bar{\chi} - \chi}{\Theta} \quad (3.9)$$

where  $\chi$  is the vapour mass fraction,  $\bar{\chi}$  is the equilibrium mass fraction, and  $\Theta$  is the empirical relaxation time scale, already defined:

$$\Theta = \Theta_0 \alpha^a \psi^b \quad (1.25)$$

$$\psi = \frac{P_{sat} - P}{P_{crit} - P_{sat}}$$

where  $\psi$  is a dimensionless pressure; the values used for the exponents are the ones recommended by [27] for the cases whit high pressure ( $p > 10 \text{ bar}$ ):

- Time scale modeling constant  $\Theta_0 = 3.84 \times 10^{-7}$
- Vapor volume fraction exponent  $a = -0.54$
- Dimensionless pressure exponent  $b = -1.76$

### 3.2.3.5 Turbulence

The local Reynold number  $Re = \rho u D / \mu$  calculated inside the jet exceeds the  $5 \times 10^8$ , so the flow is fully turbulent. The turbulence model selected was the RANS (Section 2.1.5.1), and the closure of the system was provided the by the Realizable  $k - \varepsilon$  two-layer model, that is advised for industrial-type applications characterized by heat transfer, and provides a good compromise robustness, computational cost, and accuracy, both in fine and coarser meshes. [40]

### 3.2.3.6 Implicit Unsteady and Solution Interpolation

The Solution Interpolation model allows the interpolation of the flow quantities on new mesh during the adaptive mesh refinement. The Implicit Unsteady was selected because is the most stable transient solver [44]; the time step used was constant, equal to the one adopted by Minato [42], and for the temporal discretization was used the default 1-st order.

$$\text{Time step:} \quad \Delta t = 1\mu s$$

### 3.2.4 Initial conditions

The initial conditions are the same as the Minato's work, and the thermodynamic quantities were taken from the quasi-steady state of the Marviken CFT Test n°7 after 7 seconds from the break. The initial state sees the pipe and the vessel filled with subcooled water, with a pressure of 5MPa and an enthalpy of 1067 kJ/kg, while the open space is filled with vapor at atmospheric pressure and saturated condition.

Table 3-1 – Initial Thermodynamic State - Minato

	Pressure [MPa]	Temperature [K]
<b>Water</b>	5	519.1
<b>Vapor</b>	0.1	372.8

The initial conditions are to be implemented inside the physics continuum node, through the definition of field functions. Three main field functions are needed, for the pressure, the temperature, and the phases volume fraction:

$$p_0 = \begin{cases} 5 \text{ MPa} & x \leq 0 \\ 0.1 \text{ MPa} & x > 0 \end{cases} \quad (3.10)$$

$$T_0 = \begin{cases} 519.1 \text{ K} & x \leq 0 \\ 372.8 \text{ K} & x > 0 \end{cases} \quad (3.11)$$

$$\chi_{water} = \begin{cases} 1 & x \leq 0 \\ 0 & x > 0 \end{cases} \quad (3.12)$$

the volume fraction of the vapor can be calculated as  $\chi_{vapor} = 1 - \chi_{water}$

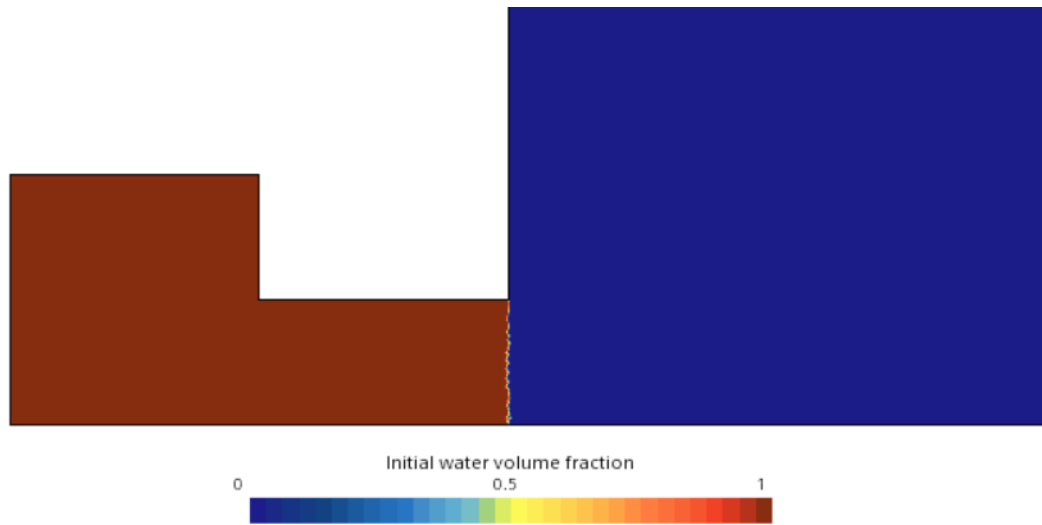


Figure 3-5 – Initial water volume fraction

### 3.2.5 Boundary conditions

A boundary type needs to be set for each Region boundary:

#### 3.2.5.1 Inlet

Under the hypothesis that the water inside the pressure vessel is at rest, the thermodynamics conditions correspond to the stagnation conditions, so for the inflow boundary it was selected the *Stagnation Inlet* boundary type. This asks for the definition of the Total Pressure and Total Temperature, together with the Supersonic Static Pressure, used to calculate the velocity of the flow inside the simulation in the event the inlet reaches the sonic or supersonic conditions. To keep the original pressure and temperature information at the inlet, the values reported in Table 3-1 for the water were used as static values, while the total values were calculated according to:

$$\frac{p^o}{p} = \left(1 + \frac{\gamma-1}{\gamma} M^2\right)^{\frac{\gamma}{\gamma-1}} \quad (3.13)$$

$$\frac{T^o}{T} = 1 + \frac{\gamma-1}{\gamma} M^2 \quad (3.14)$$

where  $p^o$  and  $T^o$  are the Total Pressure and Temperature,  $p$  and  $T$  are the static quantities,  $M$  is the Mach number calculated at the inlet, and  $\gamma$  is the ratio of the specific heats. Turbulence intensity and turbulent viscosity ratio were left with the default parameters, while the volume fraction was set to simulate the inflow of just water. All the conditions were assumed to remain constant throughout the simulation, that is limited to a few tens of milliseconds.

### 3.2.5.2 Outlet

For the outflow border, the *Pressure Outlet* boundary type was selected: it asks for the specification of the static pressure and the volume fraction, but automatically deals with the calculation of the flow direction.

### 3.2.5.3 Symmetry plane and walls

The *Symmetry Plane* boundary type applied to the lower edge of the region allows the halve of the computational domain for symmetric flows geometries.

The other boundaries were set as *Wall*, with a No-Slip shear stress specification, a Smooth surface specification, and an Adiabatic thermal specification.

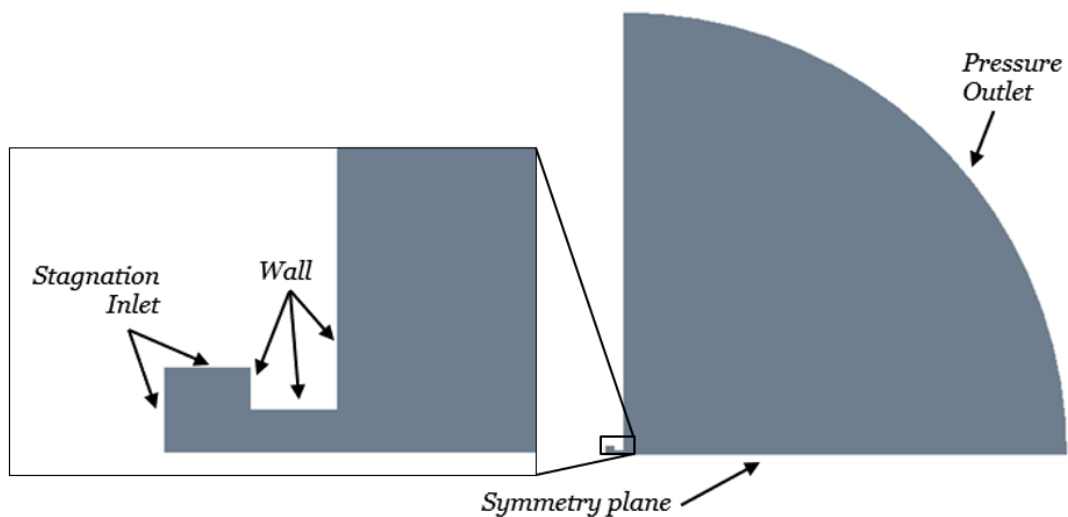


Figure 3-6 – Boundary conditions - Minato

### 3.3 Model validation

The solutions of the simulation are compared against the solutions proposed by Minato et al. The two-phase flow structure is analysed throughout its development, reporting the results for three time instants: at 1, 10, and 40 milliseconds. The paper does not provide numerical data, so the comparison is performed graphically, in a qualitative manner. Figure 3-7 shows the void fraction distribution: the dots in the technical report are proportional to the density of the volumetric liquid fraction. The model developed in this work does not directly provide the void fraction field function, so it has been defined starting from the phases density, according to the equation:

$$\alpha = \frac{\rho_l - \rho}{\rho_l - \rho_g} \quad (1.24)$$

The flow development shows that the flashing started at the pipe exit, generating an interface between the water and the two-phase mixture, that travelled through the pipe from the exit toward the vessel. At 10 milliseconds it can be appreciated the vapor annulus that forms in correspondence of the pipe inlet, due to the contraction of the flow entering from the vessel. At 40 milliseconds the flashing inception has travelled all the way up to the pipe inlet, generating a triangular (conical) liquid core. All three situations were well resolved by the model.

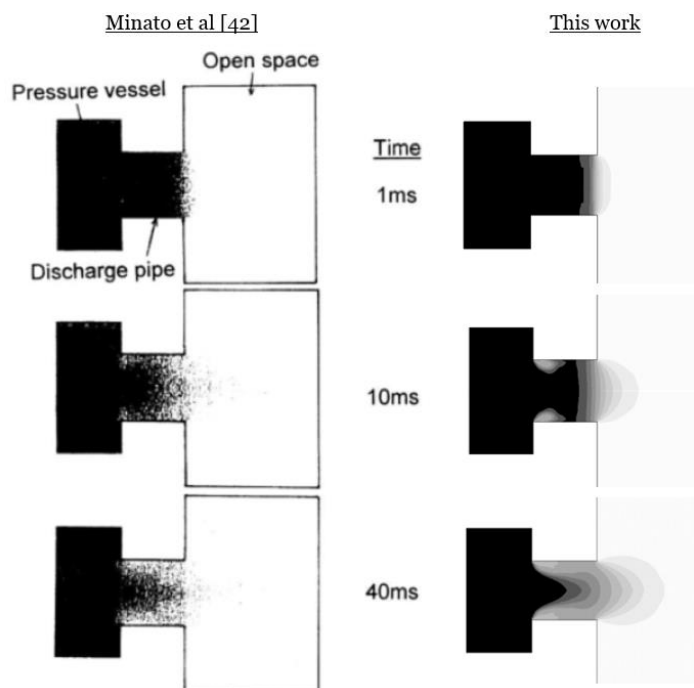


Figure 3-7 – Void fraction comparison

Figure 3-8 presents the pressure field comparison; the numerical solution calculated presents a general agreement with the results proposed. The 1 millisecond pressure field shows a poorly defined solution, deriving from the pressure wave structure that travel back the pipe after the “break”, and generates a disorganized velocity field, that is not well resolved and smoothed until approximately 5 milliseconds; several attempts with different mesh resolution and smaller time steps returned the same problem. The pressure distribution reproduces the same structure seen for the void fraction, with a high pressure core in correspondence of the liquid core, and a lower pressure annulus near the pipe inlet. The solution presents furthermore the classic flashing jet behaviour, where the volume expansion due to the rapid evaporation of the liquid near the pipe outlet, prevents the over-depressurization of the two-phase mixture inside of it, keeping the flow above the ambient pressure, and avoiding the formation of the characteristic structures of the under-expanded jet (Section 1.4.3), that is the compression and expansion waves, and the barrel shock.

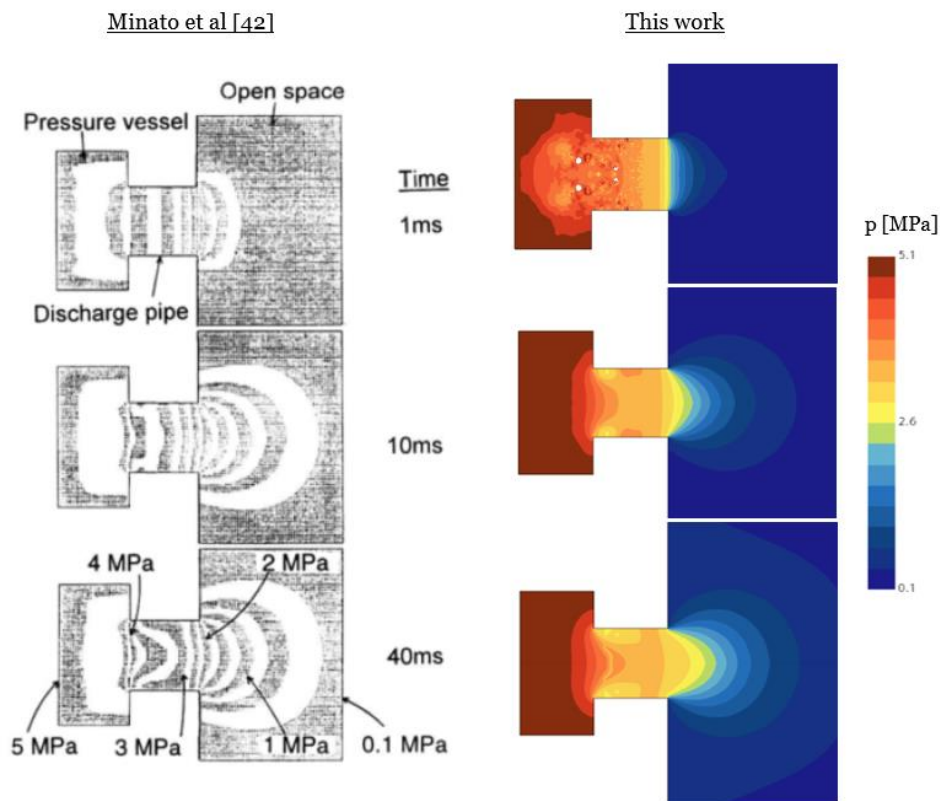


Figure 3-8 – Pressure field comparison

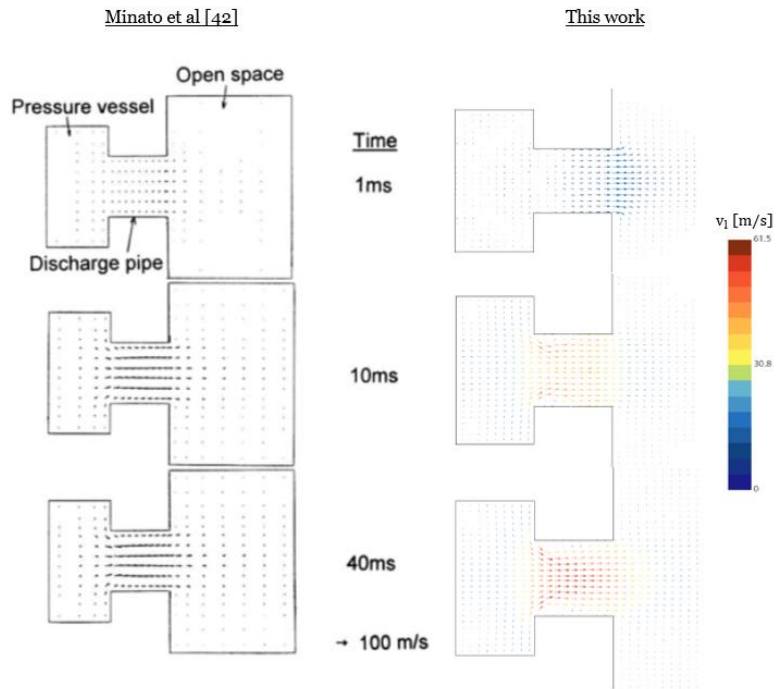


Figure 3-9 – Water velocity comparison

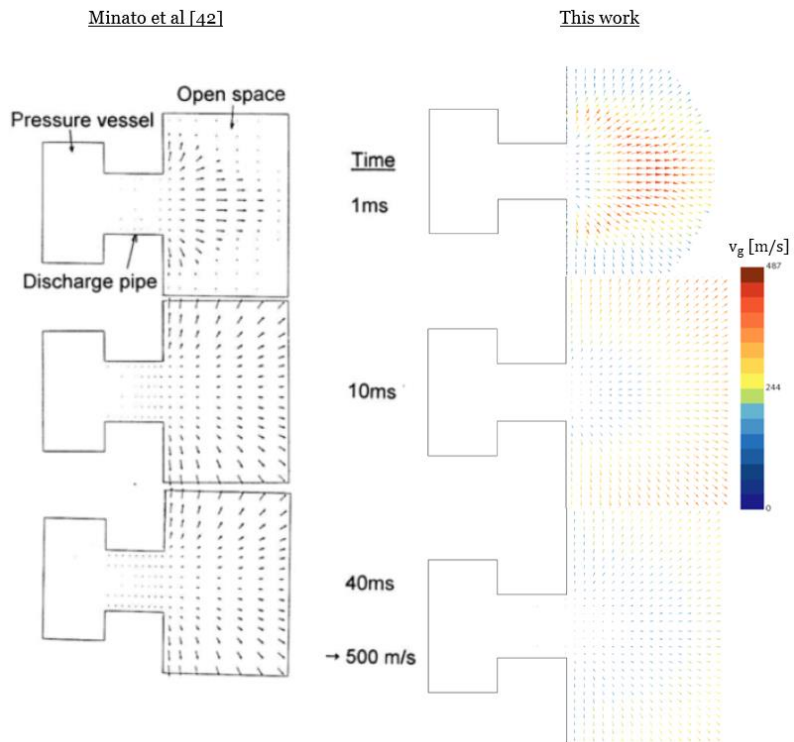


Figure 3-10 – Vapor velocity comparison

Figure 3-9 and Figure 3-10 show the vector velocity field respectively of the liquid and gas phase. In the technical report the velocities are illustrated by arrows with a length proportional to the velocity magnitude, with an indication of the maximum velocity reached by both the liquid and the gas phase. In the water velocity field, at 10 and 40 milliseconds, is noticeable the contraction of the flow at the pipe inlet, and a progressive acceleration with time. The gas velocity field at 1 millisecond shows the initial flashing and acceleration of the vapor, and the progressive expansion of the flow structure. The model produced a good agreement in the velocity distribution, with a slight under-estimation of the maximum values: -38.5% for the liquid, and -2.6% for the vapor. It is worth noticing that the model does not adopt a slip-velocity formulation, so the velocities of the phases has been weighted using the void fraction.

The mass flow rate transient at the pipe inlet is shown in Figure 3-11, and presents a good agreement with both the technical report results, and the experimental data of the Marviken CFT. The rate presents a little delay at the beginning of the discharge, as the pressure waves need to travel along the pipe, then the flow rate increase is withheld by the vapor bubble growth and expansion. A steady discharge value is reached after about 15 milliseconds, and is consistent with the steady discharge rate of the Marviken Test.

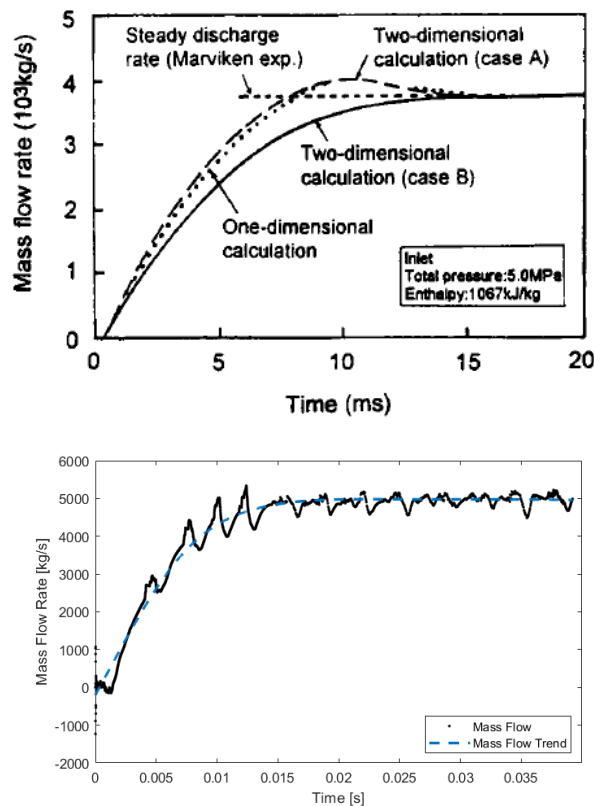


Figure 3-11 – Mass flow rate - pipe inlet

# 4 Model application to an EU DEMO LOCA scenario

## 4.1 General scenario

The scenario that we want to analyse with this model is a 2D schematization of a Loss-of-Coolant-Accident inside the Vacuum Vessel of the EU DEMO fusion reactor. The accident occurs when some unpredicted event causes the break of a section of the water-cooled lithium-lead breeding blanket (WCLL-BB), releasing the high-pressure subcooled water inside the plasma chamber, in the form of a two-phase flashing jet.

This simulation aims to investigate the adaptability of the model developed to the parameters of the real-case scenario, and identify potential improvements. It will focus on the simulation of the physical phenomenon in a reliable way, analysing the development of the flow, and the scalar field of the various calculated quantities. In particular it will focus on how the flow structure is modified by the presence of a wall in front of the break.

## 4.2 Model adaptation

The model needs to be modified in order to better conform to the geometric characteristics of the vacuum chamber, and the initial conditions of the two phases are to be substitute with the real-case thermodynamic quantities.

### 4.2.1 *Geometry and Mesh*

This model represents a preliminary study of a more complex problem, so the geometry selected for the simulation represent a simple schematization of the plasma chamber section: both the internal and external wall curvature has been neglected, while the distance between the two wall was extrapolated from Table 1-1 as the difference between the major and minor radius. In a real-case scenario, the static pressure inside the chamber would increase during the discharge, as the vapor fills the whole volume; in a 2D simulation

the pressurization of the chamber is not interesting, as the domain simulated is not correlated to the real volume. For this reason, the upper boundary of the chamber has been placed far away, in order to avoid wave reflection, and defined as outlet. The computational domain has been simulated as axisymmetric; the general configuration and dimensions are represented in Figure 4-1.

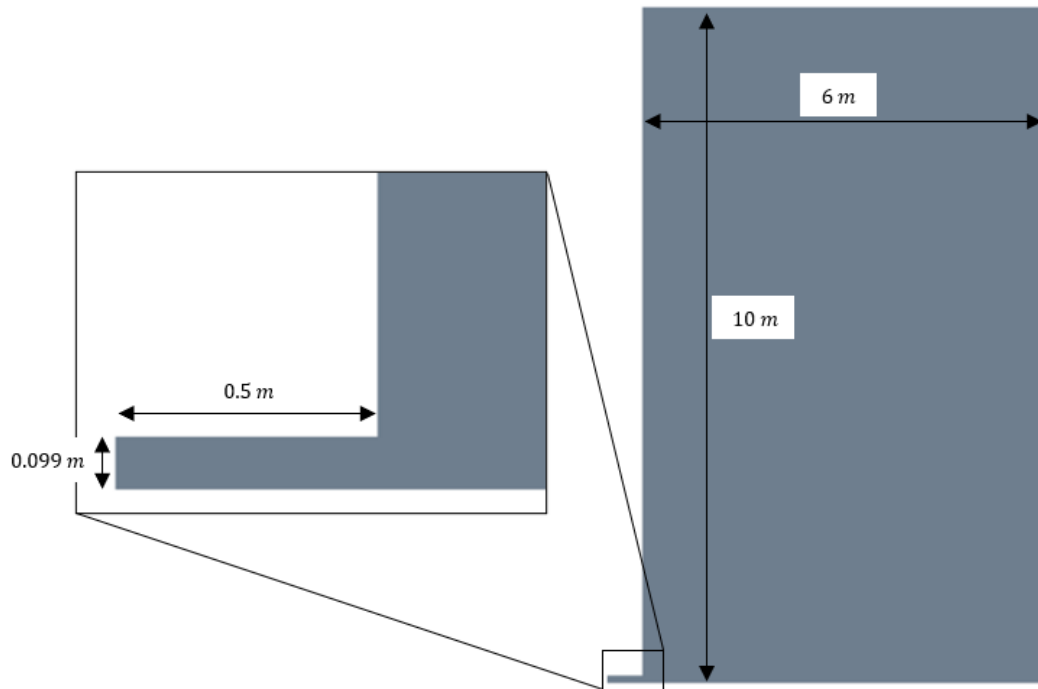


*Figure 4-1 – Geometry and dimensions - DEMO*

The inlet portion has been modified in this manner: the vessel chamber was removed, and the pipe length was increased. The pipe final length turned out to be a simulation stability requirement, as several attempts revealed that the inlet boundary needs to be away from the flashing inception point, in order to avoid the abrupt stop of the simulation, with the report of an unknown floating-point error. This may be caused by the instability of the phenomenon, which may create perturbations that, moving up the pipe, reach the inlet and destabilize it. The problem was overcome increasing the pipe length, but further study of the issue is needed.

The inlet section area was defined according to the design-basis accident scenario, involving the failure of  $1 \text{ m}^2$  surface portion of the first wall (FW), condition that would cause the discharge of water from 262 cooling channels. The inlet flow area was calculated as the sum of all exposed channel sections,

for a total surface of  $\sim 0.0308 \text{ m}^2$ : considering the axisymmetric configuration of the domain, the pipe thickness was imposed equal to the radius of a circular opening with the same area.

$$\frac{D}{2} = \sqrt{\frac{0.0308}{\pi}} = 0.099 \text{ m}$$

The automatic mesh refining strategy adopted was the same as the previous model, with just a few tweaks: the representative cell dimension in an axisymmetric configuration can be better defined as:

$$\delta_{c,axisym} = \sqrt{V_c/y_c} \quad (4.1)$$

where  $y_c$  is the radial coordinate of the cell. Another change concerned the modification of the custom control volumes for the static mesh optimization. Figure 4-2 shows the updated version of the cited volumes, and the mesh adaptation at  $\sim 1 \text{ ms}$ .

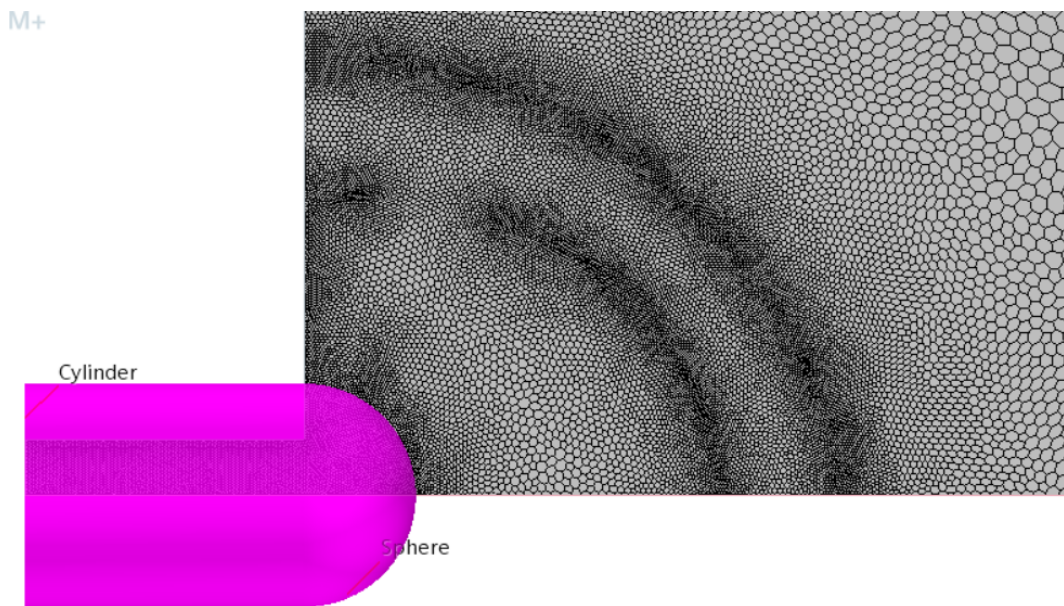


*Figure 4-2 – Custom control volumes, and mesh refinement at 1ms*

## 4.2.2 Boundary/Initial conditions

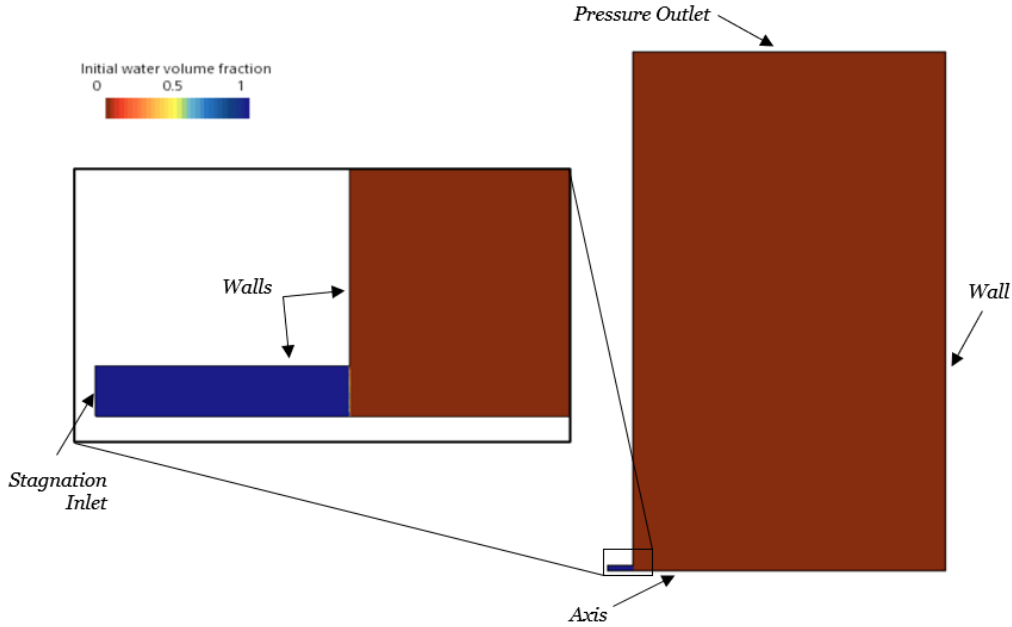


Figure 4-3 – DEMO - Initial and boundary conditions

The initial and boundary conditions are the critical aspects of this simulation: the water thermodynamic conditions inside the Breeding Blanket are displayed in Table 4-1, and correspond to the nominal condition of water inside a Pressurized Water Reactor (PWR). In those condition, water is in subcooled conditions, with a subcooling margin of  $33.3^{\circ}\text{C}$ . For computational reasons the domain cannot be empty, so the vacuum chamber was filled with saturated vapor, with a pressure calculated to ensure the respect of the continuum regime, according to the Knudsen number:

$$Kn = \frac{\lambda}{L} = \frac{k_B T}{\sqrt{2} \pi \sigma_p^2 p L} \quad (4.2)$$

$\lambda$  is the free molecular free path,  $L$  [m] is a characteristic dimension of the domain (in this case can be the distance between the inner and outer walls),  $k_B$  is the Boltzmann constant,  $T$  is the temperature of the system [K],  $p$  is the pressure of the system [Pa], and  $\sigma$  is the species particle diameter (for water molecules:  $\sigma_p = 265 \text{ pm}$ ). Navier-Stokes equation can be applied only if the continuum condition is respected, which is guaranteed for  $Kn < 0.01$ ; from this point of view, the choice for the vapor pressure is highly conservative ( $Kn \sim 10^{-7}$ ). However, during operation the VV pressure can be as low as 1-10 Pa (0.0001 – 0.00001 bar), so the simplification may impact the velocity propagation of the phenomenon (see Section 4.3.1), thus the impinging time and pressure evolution. The initial thermodynamic state of the two phases leads to an initial expansion ratio equal to 1550.

Table 4-1 – Initial Thermodynamic State - DEMO

	Pressure [bar]	Temperature [K]
<b>Water</b>	155	584.7
<b>Vapor</b>	0.1	318.96

Exactly as in the Minato's configuration, the initial computational domain is filled with water up to the pipe outlet, while the remaining portion is filled with vapor. A *Stagnation Inlet* boundary type was used for the pipe inflow, and the upper boundary of the vacuum chamber was set as *Pressure Outlet*. All the walls implemented a no-slip shear stress specification, a smooth surface specification, and an adiabatic thermal specification. The lower boundary was defined as *Axis*.

### 4.2.3 Models and Solvers tuning

The physics models used for the simulation of the flashing phenomenon are the same of the previous case, with some additions:

- Axisymmetric
- Adaptive Time-Step
- Eulerian Multiphase
- Volume of Fluid (VOF)
- Multiphase Interaction
- Multiphase Equation of State
- Segregated Flow
- Segregated Multiphase Temperature
- Implicit Unsteady
- Turbulent
- Reynolds-Averaged Navier-Stokes
- K-Epsilon Turbulence
- Solution Interpolation
- Gradients

The axisymmetric approach was selected in place of the Two-Dimensional, to bring the model closer to a 3D solution. The axisymmetric model simulates the computation on a circular sector of the domain, 1 radian wide.

The phenomenon is characterized by a fast variation of the flow topology, and presents a much larger initial pressure ratio compared to the previous case, so in order to improve the stability of the simulation and the accuracy of the results, a time-step adaptation scheme was activated. The Adaptive Time-Step model allows the automatic adjustment of the time-step: depending on the physical model activated, different time-step providers are available, all with a different criterion for the evaluation of the more suitable time-step. The provider selected for the simulation is the *Convective CFL Condition*, advised for transient flow problems [40]: it asks for the specification of a mean and a maximum CFL number (3.1), and limits the time-step so that the simulation's CFL number approaches whichever returns the minimum time-step. The values used for the simulation are reported in Table 4-2. The starting time-step value was selected, with a conservative approach, very small: equal to  $10^{-9}$ . Furthermore, the time-step change factor, i.e., the rate at which the model adjusts the time-step value, was reduced to 1.1 in order to promote a smoother transition.

Table 4-2 – Convective CFL Condition parameters

Target Mean CFL Number	0.01
Target Max CFL Number	0.1

Several simulation attempts made clear that, to support the simulation stability, it was necessary to modify some solvers' parameters:

- For all the solvers (Segregated Flow, Segregated VOF, Segregated Energy, K-Epsilon Turbulence, and K-Epsilon Turbulence Viscosity) the Algebraic Multi-Grid (AMG) Linear Solver Cycle Type has been changed from the default type to the F-cycle, disabling all the acceleration methods. The F-cycle was chosen because it performs more internal cycles among the different sub-grid levels compared to the V-cycle, but not as much as the W-cycle, constituting a good compromise between accuracy and efficiency.
- The Under-Relaxation Factors (URF) have been all set to 0.1 (with the exception of the velocity and pressure solvers within the Segregated Flow node). This benefits the convergence and the stability of the simulation, as it dampens the solution oscillations, at the expenses of the simulation convergence time.

Finally, among the stopping criteria, the Maximum Inner Iterations, i.e., the number of computational iterations the simulation performs during each time-step, was increased to 75.

## 4.3 Results and discussion

### 4.3.1 Flow development

During the first instants after the breakup, as it enters in contact with the environment pressure, the water starts to depressurize; as the pressure begins to decrease, it dives almost instantly below the saturation limit for that temperature, and the vapor starts to be generated. This happens at first on the water-vapor interface through evaporation, but as the expansion pressure waves travel up the pipe through the water, the flashing mechanism extends inside the pipe, and the vapor starts to be created within the liquid phase through boiling. Near the pipe outlet the steep acceleration of the vapor due to the flashing generates a shock wave, that then starts to propagate inside the vessel; due to the fact that the flashing is taking place on the pipe outlet, the expanding vapor is pushed in all direction, so the propagation wave assumes a spherical shape. While the shock propagates inside the chamber, it increases its superficial area, spreading its energy on a bigger surface, and as it travels through the stationary fluid inside the vessel, sets it in motion: those factors contribute to the reduction of the shock strength, which consequently decreases its velocity propagation, and the pressure, temperature, and velocity jump through it. The ongoing flashing mechanism keeps on accelerating the vapor and eventually generating other shocks waves, that during the first milliseconds of the simulation are fast enough to reach the leading wave and merge with it; but as the jet expands, those waves lose energy before doing so, and they lag behind, travelling in sequence.

Figure 4-4 displays the Mach scalar field after 7.9ms together with the axial velocity, pressure, and temperature: it reveals the presence of two spherical shock waves, at about 5.5m and 5m from the pipe outlet, and the formation of a third one at about 3m, where the flow is supersonic. The jump that the axial quantities undergo passing through the wave can also be appreciated in the figure, that shows an increase of all the three values. The pressure jump on the centreline can be used to calculate the shocks propagation velocity using the *Hugoniot* equation for the moving normal shock waves:

$$W = a_1 \sqrt{\frac{\gamma+1}{2\gamma} \left( \frac{p_2}{p_1} - 1 \right) + 1} \quad (4.3)$$

the index 1 refers to the quantities upstream of the shock (on its right in the

picture). The leading shock velocity is  $W_{LS} = 494,4 \text{ m/s}$ , equal to  $M = 1.12$ , while that of the second shock one is  $W_{SS} = 525.7 \text{ m/s}$ , equal to  $M = 1.17$ .

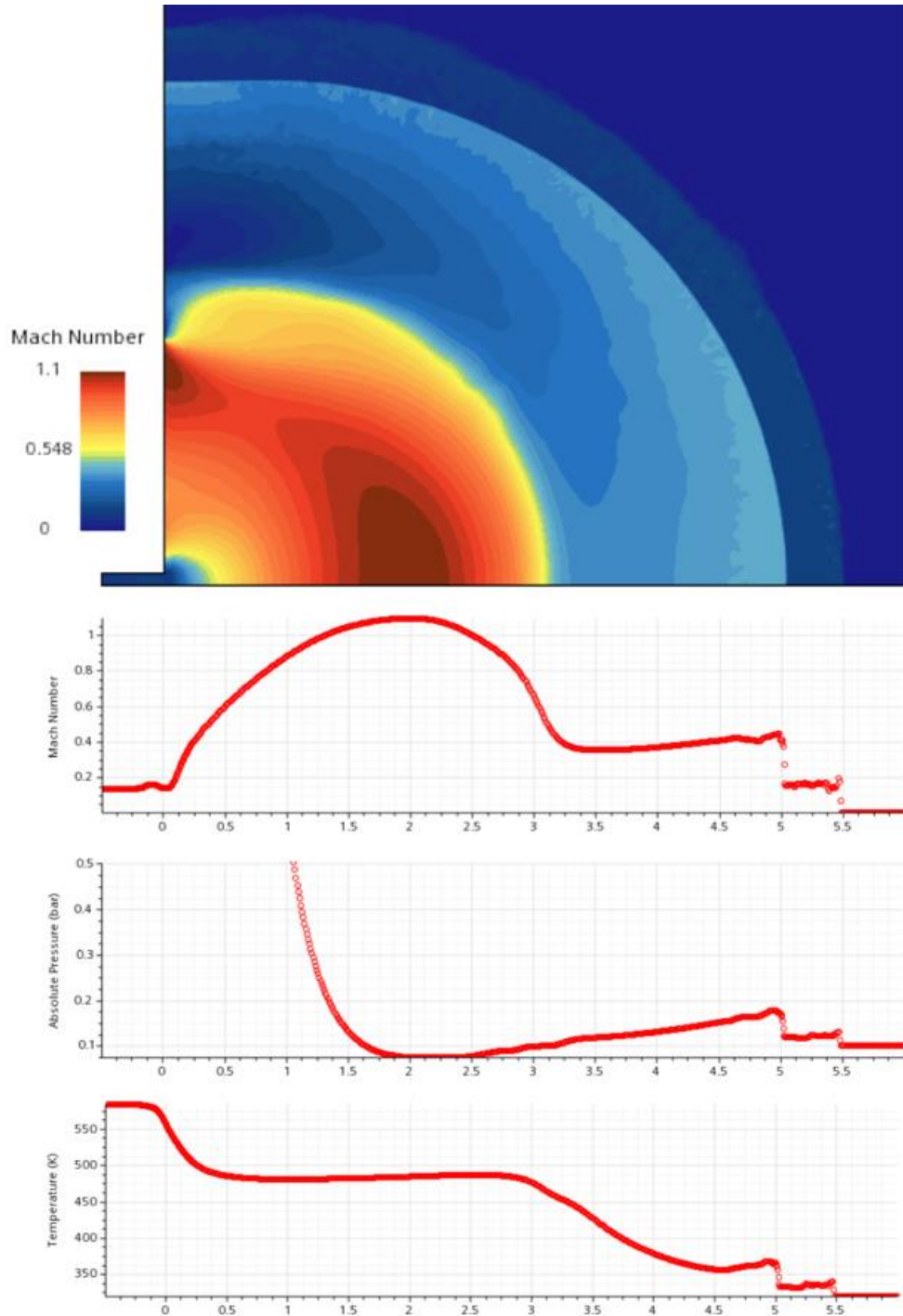


Figure 4-4 – Mach solution with axial velocity, pressure, and temperature at  $t=7.9\text{ms}$

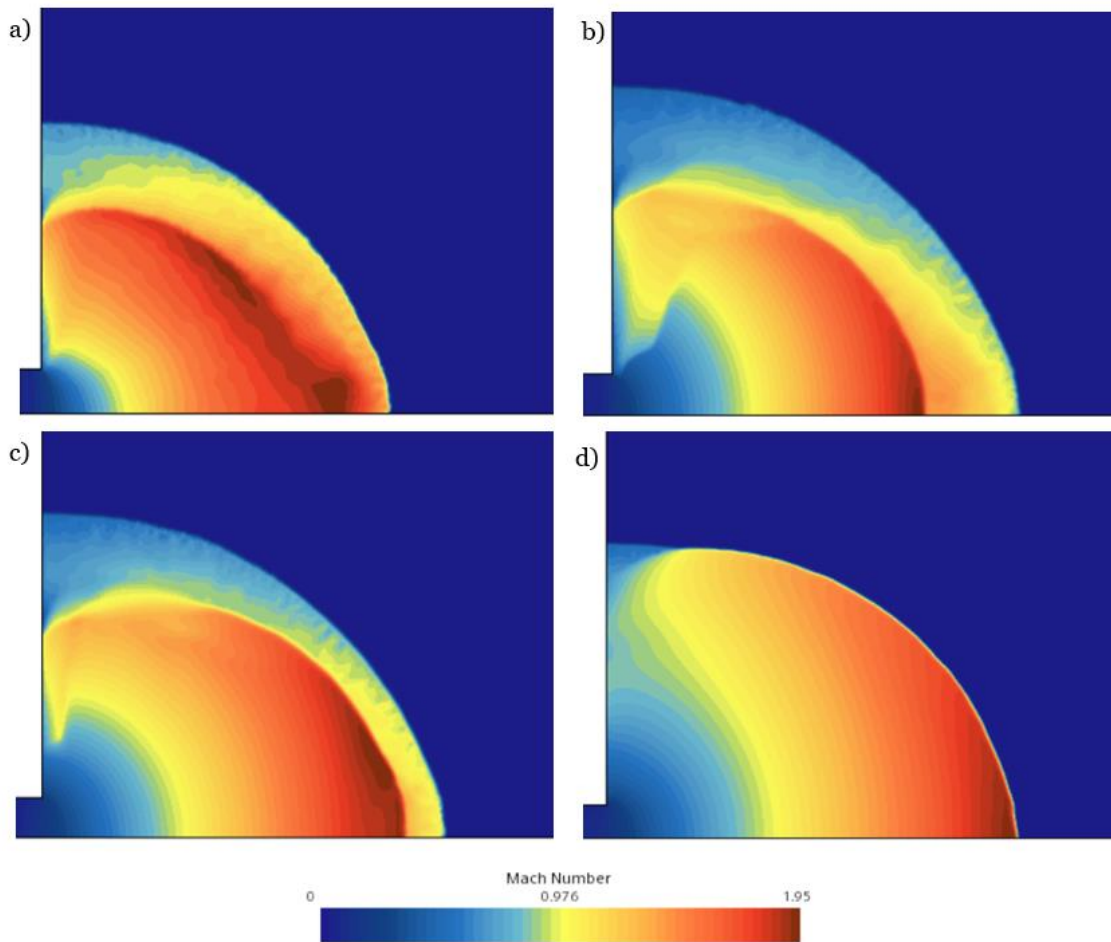


Figure 4-5 – Shock wave development and coalescence near the pipe outlet, at (a)  $t=0.88\text{ms}$ , (b)  $t=1\text{ms}$ , (c)  $t=1.1\text{ms}$ , (d)  $t=1.25\text{ms}$

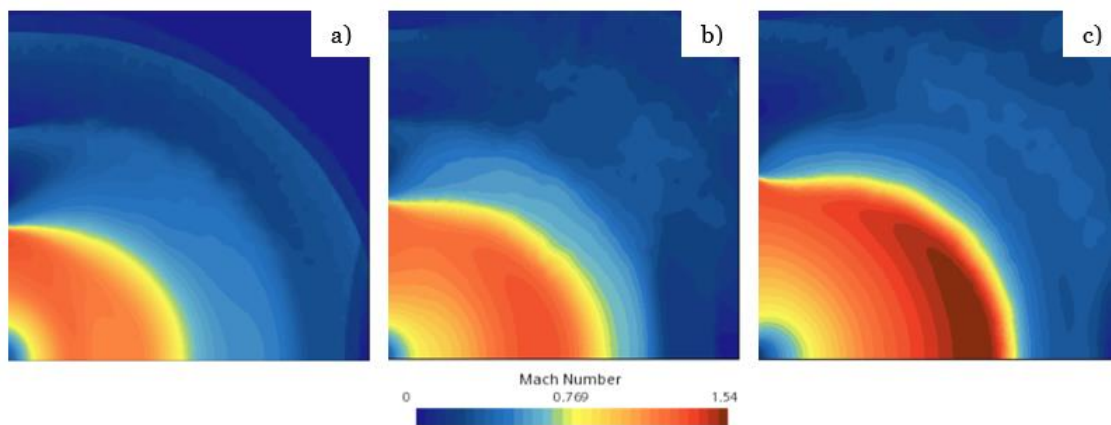


Figure 4-6 – Shock impact on opposite wall, at (a)  $t=10\text{ms}$ , (b)  $t=13\text{ms}$ , (c)  $t=16\text{ms}$

Figure 4-5 displays the generation of a shock wave inside the flow that propagates until it merges with the leading shock, in the first phases of the flow development. As it can be seen, the shocks near the pipe outlet are much stronger, and they get weakened during propagation, until they asymptotically become a pressure pulse with infinitesimal strength, i.e., an acoustic wave. [45]

At about  $t = 9ms$  the leading shock impacts on the opposite wall and is reflected back; this is consistent with the velocity propagation evaluated using the equation (4.3): calculating the shock propagation velocity at two different times ( $t_1 = 2 ms, W_1 = 511 m/s$ ;  $t_2 = 7.9 ms, W_2 = 494.4 m/s$ ), is possible to estimate the velocity decrease of the leading shock as it travels inside the vessel. With an acceleration equal to roughly  $-2847 m/s^2$ , it can be estimated an impinging time of  $t_{imp} = 8.6ms$ .

After the impinging, the flow turns outward and starts to flow parallel to the wall, preventing the shock from reaching it. Figure 4-6 displays the development of the flow after the impinging event. The reflected shock allows the preservation of the zero-velocity boundary condition, that states that the normal component of the velocity must be zero on a solid surface; behind the reflected wave the flow is stationary (Figure 4-6, a), and the static pressure can be calculated using the jump relations of the normal shock. [46] Figure 4-7 shows the direction of the flow at  $t = 23ms$ .

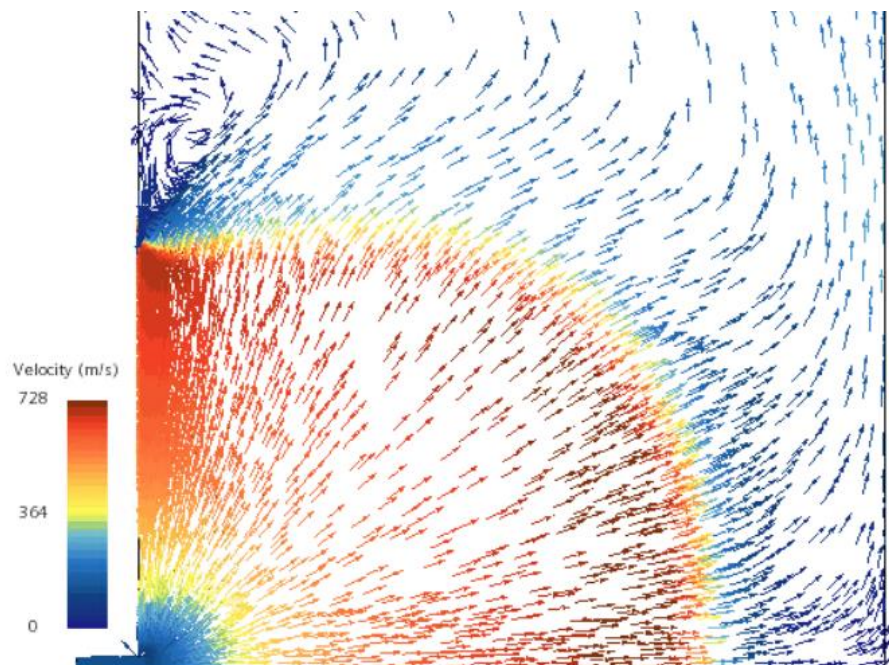


Figure 4-7 – Velocity vector field at  $t=23ms$

### 4.3.2 Pressure

The pressure solution at  $t=19\text{ms}$  is presented in Figure 4-8: it shows that inside the pipe the pressure is kept almost constant at the maximum value, as the pressure recovery rate due to the vapor generation prevents the depressurization of the liquid inside the pipe. As the water reaches the outlet, the strong flashing occurs, and the pressure quickly drops to the ambient value in about 2 meters. This demonstrates what was already mentioned in Section 1.4.4, that is, for a flashing flow the under-expansion condition can be achieved without the choking of the flow, in fact the velocity inside the pipe is constant and in subsonic condition, at  $\sim M = 0.14$ . In order to appreciate the pressure distribution inside the domain, both the scalar field scene and the pressure profile has been represented using a logarithmic scale. The area beyond the expansion region of the flow is at very low pressure, below the ambient value of  $0.1\text{ bar}$ , which is consistent with the higher velocities that characterize this area, as with the increase of the kinetic energy, the internal energy declines. At about 4 m from the pipe outlet the flow begins to be compressed again, through the formation of a now stationary shock. Between the shock and the wall, the static pressure is almost constant along the central axis, and decreases along the radial coordinate, while the flow accelerates in that direction, as shown in Figure 4-7.

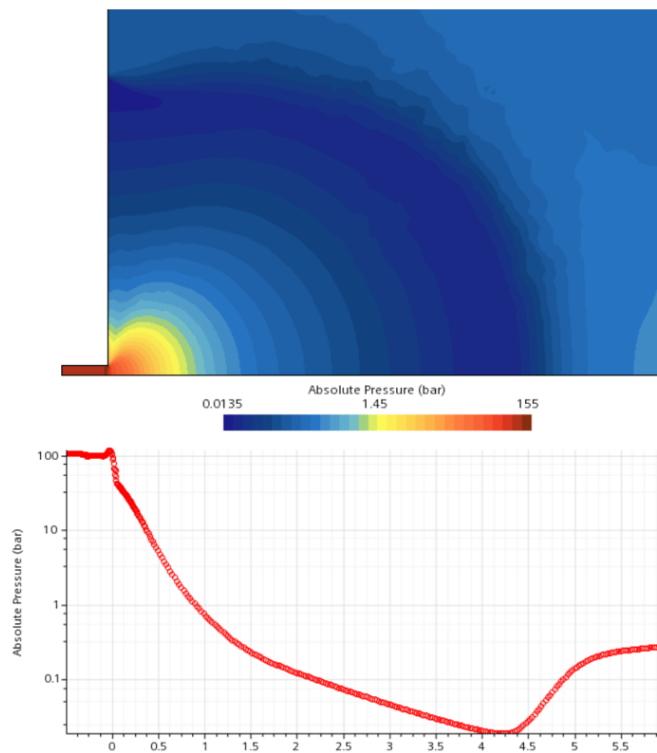


Figure 4-8 – Pressure distribution, and profile along the axis, at  $t=19\text{ms}$

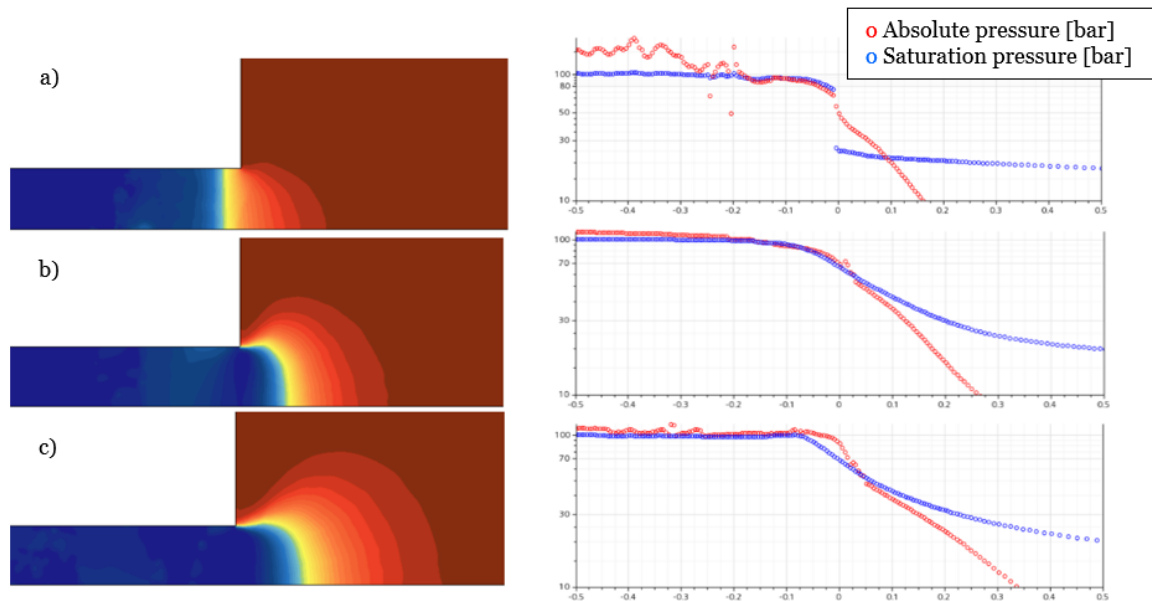


Figure 4-9 – Void Fraction (left) and Absolute pressure vs Saturation pressure (right) at (a)  $t=1\text{ms}$ , (b)  $t=7.9\text{ms}$ , (c)  $t=17\text{ms}$

In Figure 4-9 is represented the void fraction distribution (on the left), that we recall is proportional to the density of the volumetric liquid fraction, and a comparison between the absolute pressure and the saturation pressure along the jet axis, near the pipe outlet (on the right). The pressures profiles allow the qualitative identification of the flashing inception location, where the absolute pressure dives below the saturation pressure: at  $t = 1\text{ms}$  (a) the flashing occurs inside the pipe, and in fact the water-vapor interface is located at about  $-0.17\text{m}$ . At  $t = 7.9\text{ms}$  (b) the interface moved outside the pipe, and the flashing occurs at  $0.025\text{m}$ . At  $t = 17\text{ms}$  (c) the liquid core extends further inside the vessel, with the flashing located at  $0.05\text{m}$ . The presence of a liquid core outside the pipe is coherent with the subcooled initial condition of the water, that causes a delay in the vapor formation. [11] After  $t=17\text{s}$  the water-vapor interface does not advance further.

Of particular interest for this work was to monitor the variation in pressure on the wall opposite to the break. Figure 4-10 reports the pressure evolution on the inboard wall, in correspondence of the stagnation point, located on the jet symmetry axis. The first sharp rise in pressure, at  $t=9\text{ms}$ , represents the impact of the leading shock wave, and brings the pressure to the value imposed by the reflected shock wave to satisfy the zero-velocity boundary condition: in other words, the fluid downstream of the leading wave is moving at a certain velocity  $u_D > 0$ ; when the wave impinges on the wall,

the normal velocity on it should be equal to  $u_D$ , but it is not physically possible, because the normal velocity component on a solid surface must be zero, so a reflected shock wave (that travels to the left) instantly forms, with a strength such to impose a downstream velocity  $u_D = 0$ . The pressure on the wall is the one imposed by the jump conditions through the reflected wave. The same thing happens at  $t = 9.6ms$  with the second wave, that brings the pressure at the higher value  $p = 0.28 \text{ bar}$ . As displayed in Figure 4-6, the reflected waves then travel backward and stop the other incoming waves from reaching the wall, generating a stationary compression zone. Beyond this zone the flow is deflected outward, and the pressure registered is the stagnation pressure of the flow in that region.

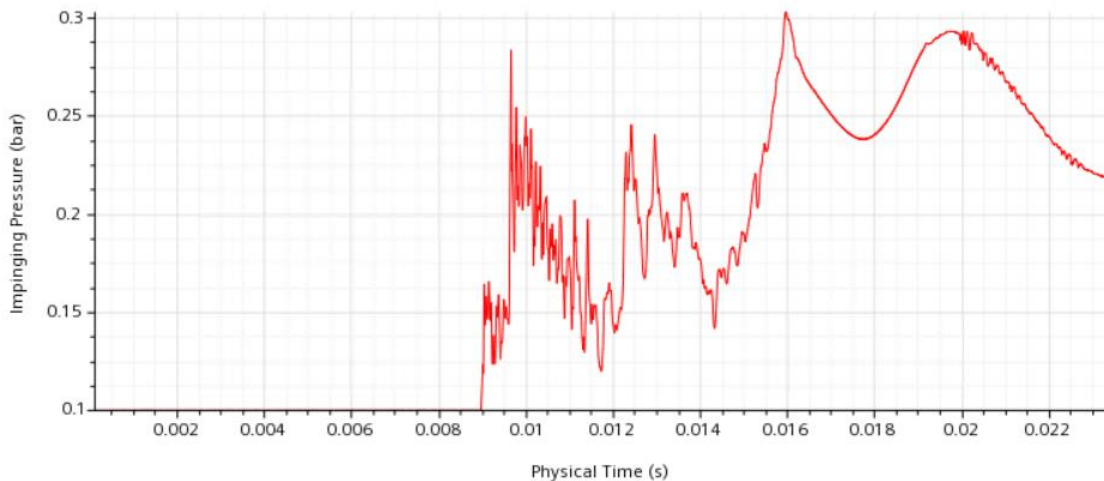


Figure 4-10 – Pressure evolution on wall opposite to the break

### 4.3.3 Temperature

The temperature solution at  $t=19ms$ , illustrated in Figure 4-11, presents along the centreline a behaviour similar to that of pressure: inside the pipe the temperature remains almost constant (it presents a slight decrease probably due to heat conduction inside the water), and then rapidly decays from the pipe outlet, and reaches a minimum value  $T_{min} = 445 \text{ K}$  in correspondence of the location of maximum velocity, after about 3m. This location is known as Minimum Temperature Distance (MTD) and is important for the flashing analysis as it represents the point where the nucleation and boiling influence cease, and the flow behaviour is governed by the evaporation and mechanical processes. After this point the temperature rapidly rises in the region characterized by the compression, and then decreases to reaches the wall value.

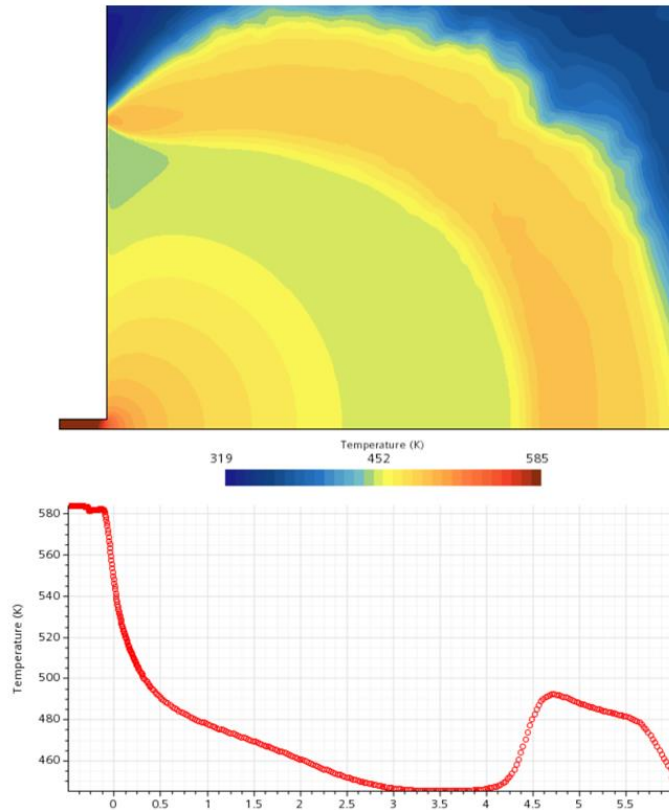


Figure 4-11 – Temperature distribution, and profile along the axis, at  $t=19\text{ms}$

Analysing the temperature evolution after the impingement, displayed in Figure 4-12, it can be noted an increase of the temperature values near the inboard wall, as the fluid starts to heat it. Proceeding with the simulation for longer times, the wall temperature will surely increase further, likely to the stagnation value of the impinging flow.

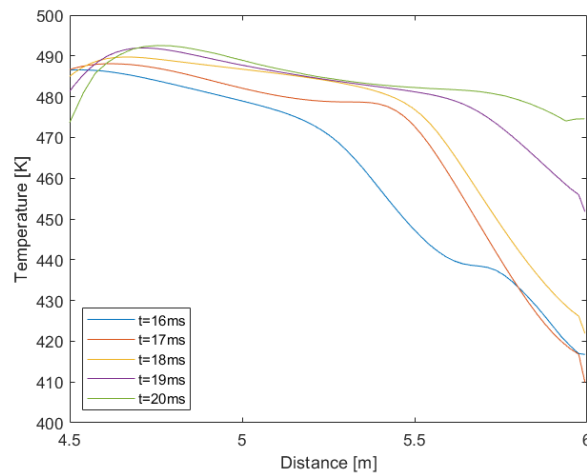


Figure 4-12 – Near Wall Temperature increase

#### 4.3.4 Comparison with the HCPB case

As stated in Section 1.3.2, two main breeding blanket design concepts are currently being investigated: the WCLL (Water-Cooled Lithium-Lead), and the HCPB (Helium-Cooled Pebble Bed). The present work analysed a simplified 2D configuration of the in-Vessel Loss-of-Coolant-Accident caused by the failure of the WCLL-BB first wall (FW), while the HCPB case has been studied by Zappatore et al. in [44].

In their work they conducted a 3D transient CFD analysis, simulating the loss of gaseous helium inside the VV. The helium used as coolant flows inside the BB channels at the nominal pressure of 80 bar, and at a temperature of  $573 \div 793$  K. They performed the simulation using an *Unsteady Implicit Coupled* model, implementing an adaptivity strategies for both the time-step and the mesh. The “Stagnation Inlet” was used for both the Pressure and Temperature boundary condition, while the inlet was dimensioned to simulate the failure of a  $5 \text{ m}^2$  portion of the FW. When the helium is released against a pressure ratio of 800, it generates a hypersonic flow inside the vessel, that impinges on the opposite wall, and pressurize the VV up to the safety threshold, that is the maximum allowable pressure on the gyrotron diamond window: 2 bar.

The main difference between the jet resulting from the release of helium, from that due to the release of water, is that the helium does not undergo a phase change, meaning that is not characterized by a flashing mechanism, but on the contrary behaves like the highly under-expanded single-phase jet described in Section 1.4.3, developing a “barrel shock” configuration. Within the limits of the comparison between a 2D simulation and a 3D one, the results differences are remarkable:

- As said, upon the release, the helium under-expanded jet develops a single cell diamond shock pattern, that expands inside the vessel with hypersonic velocity, with a maximum in the transient phase up to  $M=50$ , and impacts on the opposite wall in less than 3ms: the higher velocity and lower travel time means that the leading shock is still very strong when it reaches the wall, transferring a greater amount of energy on the surface. Furthermore, the flow at the inlet is choked, meaning that the helium enters the vessel already at sonic velocity, and its development is mostly axial, so there is even less energy dispersion. On the contrary, the flashing allows the support of the under-expanded condition without a choked inlet, so the vapor enters the vessel at a much lower velocity, and the flow expands in all directions, taking a little less than 10ms to reach the opposite wall, with a leading wave that upon arrival is almost acoustic.
- Concerning the pressure, in the helium case they simulated a closed 3D domain, allowing the study of both the local pressure peaks on several point of interests located on the chamber walls, and the average pressure

rise due to the vessel pressurization. The comparison of the evolutions of the pressure on the wall in front of the rupture for the two cases, shows a maximum pressure peak of 3.5 bar for the helium, against the increase to 0.3 bar for the water. However, the upward pressure trend recorded in the helium case cannot be compared, since helium sees an increase in the average pressure of the vessel, while the water case does not.

- The temperature fields present a similar behaviour in the two cases, with a first rapid decay, followed by a low temperature region characterized by high velocities, and then a rise due to compression mechanisms, with a final increase in front of the wall due to the flow deceleration and stop. The temperature ranges, on the other hand, are quite different: the helium is injected at >600 K, during the expansions cools down to a few tens of K, and then the temperature rises again to ~800 K, with a stagnation temperature on the wall close to 1000K. For the water the situation is quite different (see Figure 4-11 – Temperature distribution, and profile along the axis, at t=19msFigure 4-11), with the maximum temperature decrease going from 584 K to 445 K, and a stagnation temperature not yet defined, but relying on the trend simulated, it will likely stabilize to a value in the order of ~500 K.

## Chapter 3

# 5 Conclusions

This work presents a preliminary analysis of the flow generated by the accidental release of high-pressure water, used as coolant in the WCLL-BB inside the EU DEMO fusion reactor. The main focus was to simulate the flashing mechanism that takes place when the high-pressure subcooled water enters in contact with the low-pressure environment inside the plasma chamber. The process generates a two-phase jet that accelerates due to the expansion powered by the rapid evaporation of the water, and advances inside the vessel through a shock-wave structure.

A 2D unsteady CFD model has been developed, using a Eulerian multiphase approach, implementing a Volume of Fluid (VOF) model, with a Homogeneous Relaxation Model (HRM) for the phase interaction. The VOF model allows the simulation of problems where the two phases are separated by an interface, through which all the phase interactions take place, while the HRM was suitable for the simulation of thermal non-equilibrium vaporization mechanisms, treating the transition from the non-equilibrium to the equilibrium state as a relaxation process.

The 2D model has been validated against a comparable numerical problem taken from the literature, with a similar geometric configuration, but less prohibitive initial thermodynamic conditions: the results returned a good agreement.

The model has been then applied to the WCLL-BB scenario, simulating the development of a water-vapor flashing jet, characterized by an initial pressure ratio of 1550. The results have been then compared with those obtained with the 3D transient analysis of the HCPB-BB accident scenario, showing that a water release presents lower impingement pressure on the wall opposite to the break.

Further development of the model may involve the implementation of a Lagrangian approach to simulate the presence of water droplets inside the jet, in order to study their effects on the flow development, and a bubble generation model inside the liquid phase, that may affect the location and timing of the flashing inception. Furthermore, the assumption that the vessel was filled with vapor at 0.1 bar was an important simplification, as real-case chamber is filled with plasma at even lower pressure, through which the expansion shock waves may travel differently.

Finally, the transition to the 3D configuration will create a model more representative of the real scenario: the closed 3D domain is expected to have an important impact on the development of the flow, that being able to spread in all direction will likely present a different behaviour, as well as the fact that an increase of the mean pressure due to the pressurization of the vessel will affect the thermodynamic properties of the vapor inside the chamber.

# Bibliography

- [1] T. Donnè and W. Morris, “European research roadmap to the realization of fusion energy,” EUROfusion Consortium, 2018.
- [2] International Renewable Energy Agency (IRENA), «Renewable Capacity Statistics 2021,» March 2021.
- [3] M. Barbarino, “A brief history of nuclear fusion,” *Nature Physics*, vol. 16, pp. 890-893, Settembre 2020.
- [4] P. Magaud, G. Marbach and I. Cook, “Nuclear Fusion Reactors,” *Enciclopedia of Energy*, vol. 4, 2004.
- [5] G. Federici, L. Boccaccini and et al., “An overview of the EU breeding blanket design strategy as an integral part of the DEMO design effort,” *Fusion Engineering and Design*, no. 141, pp. 30-42, 2018.
- [6] «THE ITER TOKAMAK,» ITER Organization, [Online]. Available: <https://www.iter.org/mach>.
- [7] G. Federici, C. Bachmann and et al., “DEMO design activity in Europe: Progress and updates,” *Fusion Engineering and Design*, no. 136, pp. 729-741, April 2018.
- [8] A. Del Nevo, E. Martelli, P. Agostini and et al., “WCLL breeding blanket design and integration for DEMO 2015: status and perspectives,” *Fusion Engineering and Design*, no. 124, pp. 682-686, 2017.
- [9] M. D'Onorio, F. Giannetti, M. T. Porfiri and G. Caruso, “Preliminary safety analysis of an in-vessel LOCA for the EU-DEMO WCLL blanket concept,” *Fusion Engineering and Design*, no. 155, 2020.
- [10] Y. Liao and D. Lucas, “Computational modelling of flash boiling flows: A literature survey,” *International Journal of Heat and Mass Transfer*, no. 111, pp. 246-265, 2017.
- [11] G. Polanco, A. Holdo and G. Munday, “General review of flashing jet studies,” *Journal of Hazardous Materials*, no. 173, pp. 2-18, 2010.
- [12] E. Elias and P. Chambre, “Flashing inception in water during rapid decompression,” *Journal of Heat Transfer*, no. 115, pp. 231-238, 1993.
- [13] H. Guo, L. Nocivelli, R. Torelli and S. Som, “Towards understanding the development and characteristics of under-expanded flash boiling jets,” *International Journal of Multiphase Flow*, no. 129, 2020.

- [14] J. Scott, "Aerospaceweb," 17 April 2005. [Online]. Available: <http://www.aerospaceweb.org/question/propulsion/q0224.shtml>.
- [15] M. Aamir and A. Watkins, "Numerical analysis of depressurisation of highly pressurised liquid propane," *International Journal of Heat and Fluid Flow*, no. 21, pp. 420-431, 2000.
- [16] P. Bricard and L. Friedel, "Two-phase jet dispersion," *Journal of Hazardous Materials*, no. 59, pp. 287-310, 1998.
- [17] T. Gemci and et al., "Flash atomization of water/acetone solutions," *Atomization and Sprays*, no. 14, pp. 459-475, 2004.
- [18] G. Pinhasi, A. Ullman and A. Dayan, "Modeling of flashing two-phase flow," *Reviews in Chemical Engineering*, no. 21, pp. 133-264, 2005.
- [19] M. Alamgir and J. Lienhard, "Correlation of pressure undershoot during hot-water depressurization," *ASME Journal of Heat Transfer*, no. 103, pp. 52-55, 1981.
- [20] E. Kumzerova and A. Schmidt, "Effect of bubble nucleation mechanism on flashing flow structures: numerical simulation," *Journal of Computational Fluid Dynamics*, no. 11, pp. 507-512, 2003.
- [21] J. Riznic, M. Ishii and N. Afgan, "Mechanistic model for void distribution in flashing flow," in *Proceedings of Transient Phenomena in Multiphase Flow*, Dubrovnik, Yugoslavia, 1987.
- [22] N. Kolev, *Multiphase Flow Dynamics 2 – Thermal and Mechanical Interactions*, New York: Springer, 2005.
- [23] O. Jones and T. Shin, "Nucleation and flashing in nozzles-1: a distributed nucleation model," *International Journal of Multiphase Flow*, no. 19, pp. 943-964, 1993.
- [24] M. Plesset and S. Zwick, "The growth of vapor bubbles in superheated liquids," *Journal of Applied Physics*, no. 25, pp. 493-500, 1954.
- [25] H. Forster and N. Zuber, "Growth of vapor bubble in superheated liquid," *Journal of Applied Physics*, no. 25, pp. 493-500, 1954.
- [26] C. Brenner, *Cavitation and Bubble Dynamics*, Oxford: Oxford University Press, 1995.
- [27] P. Downar-Zapolski, Z. Biliki, L. Bolle and J. Franco, "The non-equilibrium relaxation model for one-dimensional flashing liquid flow," *International Journal of Multiphase Flow*, no. 22, pp. 473-483, 1996.
- [28] H. Richter, «Separated two-phase flow model: application to critical twophase flow,» *Internationa Journal of Multiphase flow*, n. 9, pp. 511-530, 1983.

- [29] F. Moody, «Maximum flow rate of a single component. Two-phase mixture,» *Journal of Heat Transfer*, n. 87, pp. 134-141, 1965.
- [30] H. Fauske, «Two-phase critical flow with application to liquid-metal systems (Mercury, Cesium, Rubidium, Potassium, Sodium, and Lithium), Technical report,» 1963.
- [31] J. Schröder e N. Vuxuan, «Vuxuan, Homogeneous non-equilibrium two-phase critical flow model,» *Chemical Engineering Technology*, n. 10, pp. 420-426, 1987.
- [32] V. Blinkov, O. Jones Jr. e B. Nugmatulin, «Nucleation and flashing in nozzles - 2,» *Journal of Multiphase Flow*, n. 19, pp. 965-968, 1993.
- [33] IAEA, «Thermal-hydraulic relationships for advanced water cooled reactors,» IAEA-TECDOC-1203, 2001.
- [34] S. Paruya e P. Bhattacharya, «Simulation of oscillations in boiling flow, in a natural circulation evaporator,» *Chemical Engineering Communications*, n. 196, pp. 362-390, 2009.
- [35] F. Schäfer and A. Manera, «Investigation of flashing-induced instabilities at the CIRCUS test facility using the code ATHLET,» *International Journal of Nuclear Energy Science and Technology*, no. 2, pp. 209-218, 2006.
- [36] A. Manera, U. Rohde, H.-M. Prasser e T. Van der Hagen, «Modelling of flashing-induced instabilities in the start-up phase of natural-circulation BWRs using the two-phase flow code FLOCAL,» *Nuclear Engineering and Design*, n. 235, pp. 1517-1535, 2005.
- [37] «IAPWS R7-97(2012) Revised Release on the IAPWS Industrial Formulation 1997 for the Thermodynamic Properties of Water and Steam,» August 2007. [Online]. Available: <http://www.iapws.org/relguide/IF97-Rev.html>.
- [38] L. Zhang, «Modélisation, analyse, et simulation d'écoulements en thermohydraulique par modèles 6 équations,» 2017.
- [39] S. Pope, *Turbulent Flows*, Cambridge: Cambridge University Press, 2000.
- [40] «Siemens 2021 STAR-CCM+ User Manual,» [Online]. Available: <https://docs.sw.siemens.com/documentation/external/PL20200617112215329/en-US/userManual/userGuide/html/index.html#page/connect%2Fsplash.html>.
- [41] Siemens STAR-CCM+, «Spotlight on... Multiphase Models,» 29 June 2020. [Online]. Available: [https://support.sw.siemens.com/knowledge-base/KB000031543\\_EN\\_US](https://support.sw.siemens.com/knowledge-base/KB000031543_EN_US).
- [42] A. Minato, K. Takamori and A. Susuki, «Numerical Study of Two-Dimensional Structure in Critical Steam-Water Two-Phase Flow,» *Journal*

*of Nuclear Science and Technology*, pp. 464-475, May 1995.

- [43] Studsvik Energiteknik AB, "The Marviken Full Scale Critical Flow Tests Summary Report," Nykoping, Sweden, 1982.
- [44] A. Zappatore, A. Froio, G. Spagnuolo and R. Zanino, "3D transient CFD simulation of an in-vessel loss-of-coolant accident in the EU DEMO fusion reactor," *Nuclear Fusion*, no. 60, 2020.
- [45] H. Steiner e W. Gretler, «The propagation od spherical and cylindrical shock waves in real gases,» *Physics of Fluids*, n. 4, 1994.
- [46] J. D. Anderson, *Modern Compressible Flow - Third Edition*, McGraw Hill Education, 2012.